Title: Cryo-EM structure of an elusive pre-transport intermediate of the multidrug transporter BmrCD reveals modes of asymmetric drug binding

Authors: Tarjani M. Thaker[1*], Smriti Mishra[2*], Wenchang Zhou[3], Jose D. Faraldo-Gomez[3], Hassane Mchaourab[2,#], Thomas M. Tomasiak[1,#]

Affiliations:

[1]Department of Chemistry and Biochemistry, University of Arizona, Tucson, AZ, USA

[2]Department of Molecular Physiology and Biophysics, Vanderbilt University, Nashville, TN, USA

[3]Theoretical Molecular Biophysics Laboratory, National Heart, Lung, and Blood Institute, National Institutes of Health, 50 South Drive, Bethesda, MD 20892, USA

*These authors contributed equally to this work

[#]Correspondence to: tomasiak@arizona.edu; hassane.mchaourab@vanderbilt.edu

Abstract: Vectorial substrate efflux by ATP binding cassette (ABC) transporters, which play a major role in multidrug resistance, entails the ATP-powered interconversion of the transporter between stable intermediates. Despite recent progress in structure elucidation of ABC transporters, a number of such intermediates have yet to be visualized and mechanistically interpreted. Here, we combine single particle cryo-EM, Double Electron Electron Resonance (DEER) spectroscopy with Molecular Dynamics simulations to profile and mechanistically frame the conformation of a hitherto unobserved intermediate in the context of BmrCD, a heterodimeric multidrug ABC exporter from *Bacillus subtilis.* In our cryo-EM structure, BmrCD adopts an inward facing architecture bound to both ATP and the substrate Hoechst-33342 and is capped by an extracellular domain which undergoes ATP-dependent conformational changes. A striking feature of the structure is a symmetric arrangement of the nucleotide-binding domain (NBD) in the presence of ATP whereas binding of Hoechst at two distinct sites in an acidic pocket stabilizes an asymmetric arrangement of the transmembrane domain architecture (TMD). Mutation of residues coordinating Hoechst in the structure abrogates the cooperative stimulation of ATP hydrolysis. In conjunction with previous studies, our findings suggest a mechanistic role for symmetry mismatch between NBDs and TMDs in the conformational cycle of ABC transporters. Moreover, the resolved structures of bimodally-bound drugs are of notable importance for future rational design and optimization of molecules for targeted transport inhibition of ABC transporters.

One Sentence Summary: Cryo-EM and EPR analysis reveal cooperative substrate binding in BrmCD in an architecture primed for transport.

ATP binding cassette (ABC) transporters harness the energy of ATP hydrolysis to traffic molecules across lipid membranes. Ubiquitous in all kingdoms of life, ABC exporters efflux a spectrum of substrates, most notably cytotoxic drugs[1]. Although the molecular architecture of ABC transporters invariably has two nucleotide binding domains (NBD) with two ATP binding sites (also referred to as the nucleotide binding site (NBS)) and two transmembrane domains (TMDs), a subfamily has evolved a catalytically-impaired NBD. Typically assembled as heterodimers, ABC exporters of this subfamily are distinguished by an asymmetric duty cycle of the motor domain where ATP hydrolysis is primarily carried out by the active ATP binding site[1], also known as the consensus NBS. The mechanistic implications of the asymmetric ATP turnover continue to be an active area of investigation.

Owing to the widespread application of single particle cryo-EM, the structural biology of ABC exporters has witnessed rapid advances in the last few years yielding snapshots of transporters in distinct conformational states. Most notably, a complement of such states was resolved for a bacterial ABC heterodimer, TmrAB[2]. These included inward-facing (IF), occluded and outward-facing (OF) conformations, and for the first time a post-hydrolysis low energy state where asymmetric binding of ATP and ADP was resolved. Current models of ATP-driven transport posit that ABC transporters rest in an inward-facing open conformation with NBDs slightly separated for high affinity substrate and nucleotide binding, though recent studies report nucleotide binding in this architecture is constitutive at least in exporters[1]. The ATP-substrate-transporter complex is then in a state favorable for transport once both NBDs are aligned to form an intact ATP hydrolysis pocket. Conserved loops (Walker A, Walker B, P-loop), present in most ATPases, and motifs (Q-loop) that are specific only to ABC transporters coordinate the positioning of a catalytic water by a highly conserved glutamate residue in the Walker B motif resulting in ATP hydrolysis and the subsequent reset of the transport cycle.

Despite the success of the TmrAB investigation in linking intermediates of ATP hydrolysis to distinct conformations, significant mechanistic gaps remain. One critical gap pertains to the sequence of events that occur prior to transition to OF conformations after substrate and ATP binding. Except ABC homodimers, structures of ATP-bound ABC exporters almost invariably have been obtained in a catalytically-impaired background where both NBD catalytic glutamates were replaced with glutamines[2–4]. Moreover, these structures as well as those of ATP-bound TmrAB, capture outward facing or occluded conformations[3–8]. This has led to a generalized conclusion that ATP binding stabilizes the OF conformation despite evidence that the stability of such a conformation may be transporter dependent[9]. Furthermore, prior to this transition, a loaded IF intermediate bound to substrate and ATP must be postulated. Such an intermediate could be transient for TmrAB, explaining its absence in the cryo-EM maps.

A second, heterodimer-specific mechanistic gap, pertains to the nature of drug binding. Efforts to sensitize drug-resistant cells to various small molecules and chemotherapeutics by inhibiting efflux pumps such as heterodimeric ABC transporters has not yet proven successful[10,11]. In the absence of a detailed understanding of determinants of transporter/drug interactions, progress on this front remains stalled. Some insights have emerged from recent structures of P-glycoprotein (Pgp) visualizing substrates[12] and inhibitors[13] cradled in the vestibule between the TMDs with

stoichiometries of one and two per transporter, respectively. In contrast, the peptide substrate was poorly resolved in TmrAB structures precluding an analysis of the role of asymmetry in heterodimer substrate recognition, although substrate binding shifted the equilibrium towards a more open IF conformation[2].

To address these two central mechanistic gaps, we integrated cryo-EM with Double Electron Electron Resonance (DEER) spectroscopy, Molecular Dynamics (MD) simulations and biochemical analysis to determine, validate and mechanistically contextualize a pre-transport, ATP-bound, Hoechst-loaded intermediate of the ABC heterodimer BmrCD from *Bacillus subtilis*. BmrCD was selected on the basis of previous DEER analyses demonstrating that the ATP-bound IF intermediate is relatively stable[14,15]. We further stabilized this intermediate in a catalytically-impaired mutant background where putative catalytic residues in both NBDs have been replaced with glutamine. Hoechst is transported by BmrCD in inside-out-vesicles and stimulates ATP turnover of the purified transporter in detergent micelles and nanodiscs[16]. The transporter structure adopts an inward-facing conformation characterized by symmetric, yet disengaged NBDs, but structurally asymmetric transmembrane domains. DEER distributions in the mutant background reveal that the cryo-EM conformation is a minor population in the ensemble. Notably, the cryo-EM maps reveal two antiparallel Hoechst molecules bound in the IF cavity, making contacts primarily with BmrC protomer seemingly reflecting the internal symmetry of the protein structure. Micro-second MD trajectories are consistent with this interpretation, and reveal the network of polar and aromatic interactions that stabilizes both substrate molecules concurrently. The predicted binding mode and stoichiometry of Hoechst is further interrogated by functional analysis and determination of Hill coefficients in wild-type (WT) BmrCD. We found that Hoechst-mediated stimulation of ATP hydrolysis is cooperative, and mutation of residues in contact with the Hoechst molecules blunts stimulation of ATP hydrolysis. In conjunction with DEER analysis, our structure integrates a number of recent results and fills in a key gap in the mechanistic understanding of ATP-coupled conformational dynamics of ABC exporters.

RESULTS

The structure of BmrCD in the substrate and ATP-bound state adopts an inward-open architecture

The structure of BmrCD was determined using single particle cryo-electron microscopy (**Fig. 1A-C; Table 1; Supp. Fig. 1**) of a Cysteine-less (C-less) BmrCD bearing glutamine substitution of D500 in BmrC and E592 in BmrD (referred to hereafter as BmrCD-QQ). The transporter was purified into LMNG micelles which were subsequently exchanged for digitonin micelles to facilitate orientation distribution on cryo-EM grids (see methods). BmrCD-QQ for cryo-EM structure determination was pre-saturated with excess ATP and Hoecsht-33342 in order to stabilize the ligand-bound intermediate (see methods). From a final dataset consisting of nearly 4.3 million, we determined a structure to 3.5Å resolution from a final subset of 157,021 particles in an inward-facing conformation where the extracellular side is closed. The topology of the entire architecture is revealed in sufficient detail to identify the presence of two molecules of the model substrate Hoechst in a central vestibule of the TMD and a single molecule of ATP in each NBD (**Fig. 1B, Supp. Fig. 2**). Notably, we resolve the architecture of a TMD insertion in

BmrD, between TM2 and TM3, forming an extracellular cap over the extracellular gate of BmrCD which we define as the BmrCD extracellular domain (ECD) (**Fig. 1D**). Comparison of the observed geometry to the series of inward-facing structures of the closely related exporter TmrAB highlights a wider IF architecture in BmrCD with NBDs slightly separated (**Fig. 2A**) relative to the narrow inward-facing open (IFnarrow; PDB ID 6raf[17]) (RMSD 5.424 Å) or the inward-facing wide conformation of TmrAB (IFwide; PDB ID 6rag[17]; RMSD 3.624 Å), both of which are stabilized by nucleotide binding in the NBS (**Supp. Fig. 3**, **Supp. Table 2**). In comparison to other prokaryotic exporters of known structure[2,6,18–24] and related members of the ABCB[3,13,25] and ABCC[4,5] families, BmrCD geometry is most similar in architecture to the heterodimeric exporter TM287/288 asymmetrically bound to AMP-PNP in one NBS (PDB ID: 4q4a[22]; RMSD 3.135 Å) (**Supp. Fig. 4, 5, Supp. Table 3**). However, the conformation of BmrCD is unique in that it is both substrate and ATP-bound yet is inward-facing.

The ATP and Hoechst-bound IF conformation has symmetric but disengaged NBDs

Because previous structures of catalytically impaired ABC transporters have captured occluded or OF conformations[3,4,6], we characterized the ensemble of conformations using DEER distance measurements between pairs of spin labels in the impaired BmrCD-QQ background for protein solubilized in digitonin and ß-DDM micelles. Consistent with these previous studies, distance distributions in the TMD (spin label pairs 96/188 and 55/146) report a predominantly OF conformation in the presence of Hoechst and ATP although a minor IF population, which we presume is captured in the cryo-EM structure, is evident in the distance distributions (**Fig. 1D**). Corresponding DEER distributions in the WT BmrCD background previously published are shown for reference[14].

The structure presented here features symmetric NBDs, and NBSs (**Fig. 2A-C**), consistent with DEER data (**Fig. 2D**). Distance distributions between spin labels introduced in proximity to the degenerate (348/532) and consensus (440/441) ATP binding sites for the QQ background are similar to those obtained in the Vanadate-trapped intermediate of WT BmrCD (**Fig. 2D**). As previously observed for the EQ double mutants in P-glycoprotein (Pgp)[3], the D500Q and E592Q mutations present in BmrCD-QQ abrogate the asymmetry of the NBS observed under turnover conditions (solid green traces in Figure 2D) in the C-less background. The distance distributions at the NBS pairs predicted from the structure overlap with those experimentally observed in C-less BmrCD in the presence of AMP-PNP (dashed green traces in **Figure 2D**). In the structure, the geometry of ATP binding is also symmetric and adopts nearly identical conformations (**Fig. 2B,C**). The unambiguous density into which ATP was modeled appears in a canonical site for nucleotide binding that overlaps with ATP in TmrAB[2] and AMP-PNP in TM288/287[26]. In this orientation, the Walker A motif stabilizes the β–phosphate of ATP, whereas the Glutamine residue in place of the catalytic base is oriented towards the γ-phosphate in both protomers (**Fig. 2C**). Unexpectedly, the NBDs of BmrC of BmrD do not contact each other, and nucleotide binding is supported entirely by intra-domain interactions that stabilize ATP within a well-defined cleft. These results support the following two conclusions: 1) The NBD architecture of our structure is more consistent with inward-facing open populations of BmrCD that are stabilized by non-hydrolyzable

AMP-PNP and 2) this state is more symmetric in the NBDs than in WT BmrCD in the presence of Hoechst and ATP.

Architecture and ATP-dependent dynamics of the ECD domain

A unique feature that distinguishes BmrCD from other biochemically-characterized ABC exporters, is the presence of an insertion between transmembrane helix 1 (TM1) and transmembrane helix 2 (TM2), which we define as the extracellular domain (ECD). Electron Potenial Density corresponding to the ECD reveals a primarily β-stranded domain consisting of two approximate subdomains (**Fig. 1D; 3A**)**.** The ECD is positioned in an orientation that results in extensive interactions with the TMD thereby occluding the extracellular TMD bundle of both BmrC and BmrD. Analysis of the electrostatic distribution over the surface of the ECD and at ECD/TMD interface further reveal both acidic and basic patches that extend into the TMD (**Fig. 3B,C**). Notably, an acidic stretch of residues extends from the ECD to the BmrC TMD; whereas, the ECD/TMD interface in BmrD is marked by a basic stretch. Somewhat surprising is the formation of a solvent accessible, acidic cavity in the ECD. Binding of both Hoechst molecules in the BmrCD TMD is observed in a similarly acidic vestibule (see below), suggesting translocation of substrate through the TMD may proceeds via interaction with and rearrangement of the ECD.

We tested the notion of a functional role for the ECD by measuring distances between a spin label on this domain (BmrD 126) relative to the two spin labels monitoring the extracellular packing of BmrC (55) and BmrD (146) (**Fig. 3D**). The ECD/BmrC interface site (46/126) undergoes a large amplitude distance opening in the high-energy post hydrolysis state (red traces in **Figure 3**). Similarly, the 55/126 pair report a large distance change as would be expected if the ECD moved in concert with BmrD. On the other hand, we observed a small distance change between the BmrD TMD (146) and the ECD (126) suggesting ATP-coupled rearrangement of this domain within the BmrD protomer.

The ATP and Hoechst-bound IF conformation features asymmetry of the transmembrane domain

Similar to TmrAB and TM287/288, BmrC and BmrD come together to form a vestibule presumably to enable substrate binding. However, this assembly is asymmetric in the TMD of BmrCD (**Supp. Table 1**). Superposition of the BmrD TMD onto the BmrC TMD by rotation around the pseudosymmetric axis of the TMD dimer highlights an outward shift of nearly every TM in BmrC relative to BmrD on the extracellular side (**Fig. 4A**). The arrangement of the intracellular side of the TMD bundle is similarly marked by a concerted outward movement of all BmrC TM helices relative to BmrD. The intracellular side also exhibits the most substantial reorientations, specifically of TM3, 4, and 6 in BmrC which shift away from the substrate binding cavity by ~4Å relative to BmrD. The presence of several π-helices along the TMD bundle likely accommodates the independent movement of the TMD helices on the two sides of the membrane leaflet.

Comparison of the pseudosymmetric arrangement of the TMD in BmrCD to TmrAB TMD highlights similarities to wild-type TmrAB in the nucleotide-bound wide state (PDB ID: 6rag[2]) and the EQ variant in the apo state (PDB ID: 6ran[2]) (**Supp. Table 2**). Even in these related architectures, substantial differences are observed in nearly every TM of

BmrD compared to TmrA, the equivalent canonical chain in TmrAB (**Supp. Fig. 5**). Comparison of the TMD geometry to inward-open architectures observed in related ABC exporters further highlights the asymmetry of the BmrCD TMD halves (**Supp. Table 3; Supp. Fig. 5**). The structures of both apo and AMP-PNP-bound TM287/288 bear the strongest resemblance to the BmrCD TMD geometery[22,27]. Superposition of each half independently reveals nearly identical bundles in BmrC and TM287, both of which contain the non-canonical NBS and is the site of bound nucleotide in both structures (AMP-PNP in TM287). However, a comparison between the homologous BmrD and TM288 chains reveals a smaller interhelical angle between TM4/TM6 in BmrD (~50º) than in BmrC or TM287/TM288 (~60º). These differences could be due to interactions between the BmrD ECD and TMD bundle, or to the unique features of substrate binding in the BmrCD TMD.

Asymmetric binding sites of two Hoechst molecules in the TMD

Remarkably, density was observed in the TMD vestibule that is able to accommodate the assignment of not just one but two molecules of Hoechst. Calculation of a cross-correlation score was used to rationalize a parallel or antiparallel arrangement of the two molecules, with the latter scoring higher (0.65 (antiparallel) versus 0.60 (parallel)) and thus supporting an antiparallel assignment. Notably, the TMD substrate densities exhibit an asymmetric positioning relative to the pseudosymmetric axis of the TMD (**Fig. 4B**), matching the asymmetry of the TMDs. The Hoechst molecules bind in an opposite orientation to each other, an arrangement similar to the Pgp inhibitors Zosuquidar and Tariquidar in Pgp[28,29]. The Hoechst binding pockets are on each side of a secondary pseudosymmetric two-fold axis relating the NBDs, and are lined with residues primarily along the BmrC half of the TM bundle. These pocket-lining residues differ between the two halves, ie they are in non-equivalent from BmrC to BmrD (**Fig. 4D-F**), likely because the TMD segment lining the substrate vestibule itself is asymmetric (**Fig 4A**; **Supp. Fig. 5**). Nonetheless, BmrC residues L130, F134, and W290 line both pockets. Also, both pockets form a chemically similar environment, lined by aromatic residues (pocket 1 – Phe293; pocket 2 – Phe83 and Phe134) and capped by an acidic residue (pocket 1 Glu297; pocket 2 – Asp141).

Antiparallel Hoechst molecules are stabilized by analogous interaction patterns

To evaluate the interpretation of the distinct densities observed within the BmrCD transmembrane domain as two antiparallel Hoechst molecules, and to identify the specific interactions that underpin their stabilization, we turned to all-atom molecular dynamics (MD) simulations (**Fig. 4G**). Specifically, we calculated two independent 1-μs trajectories in which the transporter and the two Hoechst molecules are free to diffuse, or reconfigure, and evaluated the resulting structure in each case. For computational efficiency, we considered a protein construct that lacks the nucleotide-binding domains and the ECD inserted between TM1 and TM2 of BmrD was also truncated (**Fig. 4G**). In the cryo-EM structure, these domains contribute minimally to the BmrC-BmrD interface, which primarily involves contacts in the transmembrane domains. The simulated construct showed a high degree of similarity to the starting structure throughout the calculated trajectories, with average backbone RMSD values of 1.6 ± 0.2 Å over the last 0.5 μs. The two Hoechst molecules initially modeled also remained stably bound, each forming multiple contacts with BmrC, but barely any with BmrD (**Fig. 4H, Supp. Fig. 6**). For both

molecules, the two simulations resulted in similar poses and interaction patterns; this convergence is reassuring as it indicates both MD trajectories sample the same energetically favorable states. The information from the MD trajectories was used to fit the Hoechst molecules in cryo-EM density for an optimal placement.

Unlike the two molecules of ATP in the BmrCD NBSs, the two molecules of Hoechst are marked by different geometries (**Fig. 4C**). Hoecsht-1 (silver) is largely coordinated by residues from BmrC TM3, TM5 and TM6 and one residue from BmrD TM1 and 2 residues from BmrD TM6 (**Fig. 4E**) whereas Hoecsht-2 (green) forms extensive contacts with residues primarily from BmrC TM1, TM2, and TM3 (**Fig. 4F**).The binding pose for Hoechst-1 appears to be defined by the interaction between the piperazine group (carrying a charge of +1) and Glu297 (**Fig. 4I**). The two benzimidalole rings (which together also carry a charge of +1) form additional π-π and cation-π interactions with the rings of Phe293 and Trp290, whereas the etoxy-benzene is engaged by a T-shaped aromatic interaction with Tyr257. Hoechst-2, while oriented inversely relative to the membrane plane, is similarly anchored by ion-pairing and cation-π interactions formed by the piperazine group, namely with Asp141, Phe145 and Trp290, which is the only residue that contacts both ligand molecules in our trajectories. The benzimidalole rings in molecule '2' form additional π-π and cation-π interactions with the rings of Phe83 and Phe134, whereas the etoxy-benzene tail appears to be largely disengaged, in contrast to Hoechst-1 (**Fig. 4I**). These interactions, π-π and cation-π interactions, are reinforced by their observation in the cryo-EM structure. Interestingly, therefore, the pattern of interactions formed by the two molecules in this antiparallel arrangement also appears to reflect the internal structural symmetry of the TMDs.

Lastly, it is worth noting that these interaction patterns recapitulate what is observed in high-resolution crystal structures of other biomolecules in complex with Hoechst. In the abovementioned structure of outward-open LmrP[30], a Hoechst molecule is stabilized through ion-pairs between two acidic side chains and the piperazine and benzimidalole groups, albeit in a different orientation nearly perpendicular to the plane of the transmembrane. The ligand is however only in contact with one of the transmembrane domains, like in our structure of inward-open BmrCD. Binding of Hoechst to LmrR, a transcriptional repressor of the LmrCD drug transporter, involves aromatic stacking of tryptophan sidechains and the benzimidalole rings[31], while dipole-π and water-mediated polar interactions explain the mode of binding to DNA[32]. Our cryo-EM and MD simulation data shows that it is this interaction versatility that may enable BmrCD to recognize two Hoechst molecules simultaneously.

Moreover, the arrangement and asymmetry in geometry of the two Hoechst molecules in the cryo-EM structure and MD analysis are not without precedent and are reminiscent of the two molecules of the inhibitor zosuquidar bound to human Pgp[13] (ABCB1) where one zosuquidar molecule is extended while the other molecule is in a bent conformation (**Supp. Fig. 5**). Notably, binding of these inhibitors occurs at a site closer to the extracellular gate, which potentially supports the occluded architecture observed in Pgp. The positioning of Hoechst in BmrCD-QQ is most similar to LPS bound to MsbA and overlaps with the inner core of the polysaccharide portion of the molecule (**Supp. Fig. 5**)[20], parallel with the presumed inner leaflet of the transmembrane region.

304 **Cooperative Hoechst stimulation of ATP turnover is blunted by mutation of**
305 **coordination residues**
306 Because our structure reveals the presence of two bound Hoechst molecules, we
307 reasoned that mutual stabilization would result in cooperative binding of the drug. To test
308 this notion, we determined the k_{cat} of BmrCD ATP hydrolysis as a function of increasing
309 Hoechst concentrations (**Fig. 5A**). We observed a sigmoidal dependence of k_{cat} with a
310 Hill coefficient of approximately 1.8 (**Fig. 5B**). Not only does this data confirm
311 cooperativity, but it also mechanistically validates the binding of two Hoecsht molecules
312 by demonstrating direct coupling to ATP hydrolysis to the NBDs.
313 Conversely, mutations of residues that coordinate the substrate molecules in the
314 structure reduce stimulation of ATP turnover (**Fig. 5C**). We targeted both acidic and
315 hydrophobic residues in the cavity. Alanine substitution effects were variable but overall
316 consistent with the residues implicated in the structure. Notably, W290A which
317 coordinates both Hoechst molecules has a substantial effect on ATP stimulation.
318 Similarly, D141 in proximity to Hoechst-2 abrogates the Hoechst dependence, although
319 its basal rate is higher than for WT BmrCD. This presumably reflects a rearrangement of
320 the BmrC molecules that disrupt coupling of the TMD to the NBD.

321 **DISCUSSION**
322 The accelerated pace of structure determination of ABC exporters set the stage
323 for an almost unprecedented structure-mechanism understanding. Yet intermediates
324 predicted to be populated in the transport cycle continue to be conspicuously absent from
325 the structural record. In addition, except for TmrAB and bacterial homodimers, the
326 structure space has been dominated by transporters with impaired ATP-hydrolysis. In the
327 presence of ATP, these structures are outward-facing with no evidence of bound
328 substrates. Based on spectroscopic[14,33] and biochemical data[34], the underlying mutations
329 conspire to reshape the energy landscape further confounding the mechanistic
330 interpretation of the structural record.
331
332 The collection of TmrAB cryo-EM structures is thus far the most complete record
333 of stable intermediates on the energy landscape of an ABC exporter. However, under
334 turnover conditions of excess ATP, two predicted intermediates were missing. One is the
335 OF conformation which purportedly release the substrate, the absence of which was
336 attributed to its presumed transient nature. The structure of the OF conformation was
337 visualized in the catalytically-impaired mutant bound to ATP as well as in the vanadate-
338 trapped WT. The second, is a loaded pre-transport intermediate poised for transition to
339 the high energy OF conformation. Because previous structures of catalytically-impaired
340 ABC exporters such as Pgp[3] and Mrp1[4] were in the OF conformations, a substrate- and
341 ATP-loaded IF intermediate was not accounted for.
342
343 Here, we report the structure of this elusive substrate- and ATP-bound,
344 intermediate. Cryo-EM reveals an IF architecture bound with to molecules of the substrate
345 Hoecst-33342 in the TMD, and two molecules of ATP in the NBDs of a catalytically
346 impaired variant of BmrCD. Each molecule of Hoechst binds in a similarly located but
347 nonequivalent pocket on the C or D chain and our ATPase data support their role in
348 cooperative allosteric modulation of ATP turnover. Validated by DEER measurements in

349 the WT and the mutant, we assign this conformation to the substrate- and ATP-loaded
350 intermediate poised for transition to a high energy post hydrolysis intermediate. In the
351 case presented here, previous DEER data highlighted the stability of the ATP-bound IF
352 intermediate in BmrCD which was one of two fortuitous factors that allowed it to be
353 represented in our cryo-EM reconstruction, although outward facing states may also be
354 present. The second factor is the structural order of this intermediate which was
355 conducive to it cryo-EM reconstruction.
356
357 Our BmrCD structure unlocks details of the nature of pseudosymmetry breaking
358 in ABC transporters and stimulates hypotheses on the mechanistic roles of symmetry
359 mismatch between the NBDs and TMDs. Alignment with the recently determined cryo-
360 EM structures of TmrAB confirms that BmrCD is in a previously unobserved intermediate.
361 Distances between NBDs are most consistent with the inward-facing wide state, albeit
362 BmrCD is wider than TmrAB. Approximately 75% of BmrCD aligns with this TmrAB
363 conformation, including all of BmrC and most of the transmembrane portion of BmrD. The
364 NBD of the canonical BmrD protomer does not align, instead showing a ~40º rotation
365 around the symmetry axis of the NBD dimer.

366 The symmetry of the NBDs holds for most of the transmembrane region but is
367 broken in several locations including TM3 and TM6, especially TM6 in BmrD. TM6 is
368 noteworthy because this helix has been identified as important for substrate gatekeeping
369 in TmrAB[35] and in *C. elegans* Pgp[36]. In our structure, TM6 in BmrC and BmrD each
370 directly binds one of the two Hoechst molecules which are located in similar pockets in
371 BmrC and BmrD, showing a pseudo-symmetric arrangement. However, TM6 from BmrC
372 breaks that symmetry and is closer to TM6 of BmrC. MD simulations confirm this
373 arrangement and the stabilizing interactions that overlap with the binding mode observed
374 in the structure. We propose a direct relationship between the asymmetry of substrate
375 binding in the cavity and the overall asymmetry of the TMDs of BmrCD.
376
377 An emerging theme from structural and spectroscopic investigations of ABC
378 exporters posits a role for substrates and inhibitors in stabilizing symmetric or asymmetric
379 conformations. Cryo-EM structures of Pgp have highlighted different modes of inhibitors
380 and substrates binding with the former filling more of the substrate cavity and inducing a
381 more symmetric arrangement of the NBDs[12]. However, substrate binding induces
382 asymmetric states both in IF conformations and post-hydrolysis conformations, as
383 deduced from DEER analysis of Pgp[37]. Building on this theme, we propose that our
384 symmetry-mismatched BmrCD structure is arrested in an “inhibited-like conformation” by
385 the substitution of the catalytic glutamate in the consensus NBS. In a WT background,
386 we propose that the asymmetry would propagate from the TMD to the NBD resulting in
387 the asymmetric hydrolysis of ATP during transport. Indeed, extensive DEER
388 investigations of BmrCD under turnover conditions concluded that ATP hydrolysis in the
389 consensus NBS is coupled to asymmetric structure of the NBDs[14]. We predict that
390 subsequent or concurrent transition to an OF conformation accompanied by the
391 dissociation of the substrates resolves the asymmetry in the TMD.
392

In addition to outlining the structural features and the mechanistic context of an intermediate presumed to be poised for transport and revealing modes of substrate interactions with a multidrug transporter, our results have general implications for the field. Our structure resembles a necessary intermediate on the path from structures that have been observed with cryo-EM – a symmetric resting state without substrate loaded to asymmetric post-hydrolysis states that have released substrate. In between these states, a transition must occur that "breaks" this symmetry and bring NBDs into alignment for proper catalysis to take place in one of the two NBDs. This transition may reflect asymmetric loading of substrate and asymmetric movements in the TMDs that allosterically facilitate NBD alignment. BmrCD only has one such functional site, but a similar mechanism may be relevant for most ABC exporters, which have two such sites but which nevertheless might have a preferred order[38]. Nevertheless, the absence of intermediates in the structural record of a particular transporter may reflect the energetic idiosyncrasies of the transporter being investigated and should not be extrapolated in the context of a general mechanism. Thus, a consensus mechanism for ABC heterodimers will require the convergence of structural, spectroscopic and functional investigations of multiple transporters.

MATERIALS AND METHODS

Cloning

Cysteine-less (C-less) BmrCD in pET21b(+) was created as described previously[14]. Briefly, native Cysteines in BmrCD-WT were substituted with alanines using QuikChange site directed mutagenesis. The C-less BmrCD template was then used to generate BmrCD-QQ where the conserved glutamate of the walker B motif in the consensus site in BmrD (E592) and aspartate of the degenerate site in BmrC (D500) were substituted with glutamine (Q). Site-directed mutagenesis was also used to generate double-Cysteine mutants and substrate binding mutants. All substitutions were confirmed by DNA sequencing.

Expression and purification

C-less BmrCD and all mutant plasmids were transformed into *Escherichia coli* BL21(DE3) cells. A single colony was inoculated into 20 mL Luria Broth (LB) for the primary culture which subsequently was used to start the main culture consisting of 1L of minimal media supplemented with glycerol (0.5% v/v), thiamin (2.5 µg/mL), ampicillin (100 µg/mL), $MgSO_4$ (1 mM), and 50X MEM amino acids (1 mL). Cultures were grown at 37°C with shaking to an OD_{600} of 1.2, and the expression of BmrCD induced by the addition of 0.7 mM isopropyl β-D-1-thiogalactopyranoside. BmrCD cultures were incubated at 25°C with shaking for another 5.5 h. The cells were harvested by centrifugation and stored at −80°C. The cell pellets were resuspended in 20 mL of lysis buffer (50 mM Tris-HCl, 5 mM $MgCl_2$, 1mM EDTA, pH 7.5), including 10 mM DTT, 10 µg/mL DNase, 0.1 mM PMSF, 1/3 of a Complete EDTA-free protease inhibitor cocktail tablet (Roche) and were lysed by five passes through an Avestin C3 homogenizer at 15-20,000 PSI. The lysate was centrifuged at 9,000g for 10 min to remove cell debris and the membranes isolated by ultracentrifugation at ~200,000g for 1 h.

437 Membranes of C-less BmrCD and mutants assayed in 0.05% n-dodecyl-β-D-
438 maltopyranoside (β-DDM) were solubilized in resuspension buffer (50 mM Tris-HCl, 100
439 mM NaCl, 15% (v/v) glycerol, pH 8.0) including 1 mM DTT, 1.25 % w/v β-DDM with
440 constant stirring on ice for 1 h. The membranes of double mutants studied in 0.25%
441 digitonin were solubilized in resuspension buffer (50 mM Tris-HCl, 100 mM NaCl, 15%
442 (v/v) glycerol, pH 8.0) including 1 mM DTT and 1% w/v Lauryl Maltose Neopentyl Glycol
443 (LMNG). Solubilized membranes were then centrifuged at 200,000g for 1 h to remove
444 insoluble particulates. The solubilized fraction was then incubated for 2 h with 300 µL of
445 pre-equilibrated Ni-NTA resin (QIAGEN) in Ni-NTA buffer (50 mM Tris-HCl, 100 mM NaCl,
446 15% (v/v) glycerol, 0.05% β-DDM, pH 8.0) for ß-DDM samples or Ni-NTA buffer 2 (50 mM
447 Tris-HCl, 100 mM NaCl, 15% (v/v) glycerol, 0.005% LMNG, pH 8.0) for digitonin samples.
448 BmrCD-bound Ni-NTA resin was loaded into a gravity column, washed with five column
449 volumes of Ni-NTA buffer containing 20 mM imidazole and eluted with buffer containing
450 250 mM imidazole.

451

452 **Cryo-EM sample preparation**

453 C-less BmrCD harboring the D500Q (BmrC) and D592Q (BmrD) mutations
454 (BmrCD-QQ) was prepared cryo-EM by first exchanging sample purified by size exclusion
455 chromatography in SEC Buffer 1 (50 mM Tris-HCl, 150 mM NaCl, 0.01% LMNG, 20%
456 glycerol, pH 7.4) into SEC Buffer 2 (50 mM Tris-HCl, 200 mM NaCl, 0.06% digitonin, pH
457 7.4). Briefly, approximately 2.5 mg of SEC-purified BmrCD-QQ was buffer exchanged by
458 two rounds of 10-fold dilution with SEC Buffer 2 and concentration in an Amicon Ultra-
459 100 kDa centrifugal filters (Millipore) prior to SEC purification over a Superose 6 Increase
460 column (Cytiva) equilibrated in SEC Buffer 2 (**Supp. Fig. 1**). Fractions were pooled and
461 concentrated to a final concentration of 3.1 mg/mL measured by BCA Assay (Pierce). For
462 substrate trapping, protein was diluted to 22 µM (~2.5 mg/mL) in 50 mM Tris-HCl, 200
463 mM NaCl, 0.2% digitonin, pH 7.4 and incubated with 75 µM Hoecsht-33342 (Thermo
464 Fisher) on ice for 30 min prior to the addition of 8 mM ATP/$MgCl_2$. To initiate substrate
465 trapping, the sample was then heated for 1 min at 37˚C and immediately applied to freshly
466 glow-discharged grids placed inside of a Leica GP2 plunge freezer equilibrated to 10ºC
467 and 85% humidity.

468

469 **Cryo-EM data acquisition and processing**

470 Cryo-EM data were collected on a Quantifoil 1.2/1.3 200-mesh spacing copper grid
471 (Electron Microscopy Sciences) loaded with 5 µL of BmrCD-QQ saturated with Hoecsht-
472 33342/ATP/$MgCl_2$ (BmrCD-$QQ^{H/ATP}$) and incubated for 10 s prior to blotting on Whatman
473 1 paper for 4 s and plunge-frozen in liquid ethane. In total, 6,919 were recorded by beam-
474 image shift on a 300 kV Titan Krios microscope (Thermo Fisher) equipped with a K3
475 Summit detector (Gatan) operated in super-resolution mode (Pacific Northwest Center
476 for Cryo-EM) at a nominal magnification of 81,000X, corresponding to a pixel size of 0.54
477 Å. Dose-fractionated movies were acquired at an electron flux of 0.82 $e^{-1}/Å^2$ per frame
478 (45 frames total) corresponding to a total dose of 37.2 $e^{-1}/Å^2$. Images were recorded with
479 a target defocus range of -0.8 to 2.1 µm.

Data were processed in RELION 3.0[39] and 3.1[40]. Frame-based motion correction, 2X binning, and dose weighting were performed using MotionCor2 to generate an image stack with pixel size of 1.059 Å. Defocus values were estimated from motion corrected, dose weighted images using CTFFIND4.1[41]. Approximately 1,500 particles were manually picked from an initial subset of micrographs and subject to likelihood-based 2D classification to generate templates for automated particle picking. In total, 4,970,928 particles were picked, extracted at a box size of 288 pixels with 4.0 Å/pixel, split into 4 subsets of 1,242,732 particles, and subject to four rounds of 2D classification and particle selection to eliminate bad particles resulting in a final particle set containing 632,978 particles extracted to the full pixel size (1.059 Å/pix) for 3D classification. The best class selected on the basis of highest resolution and visible transmembrane density yielded 157,021 particles, which were then subject to iterative rounds of 3D refinement, CTF refinement, Bayesian polishing, and postprocessing in RELION to yield a final map at 3.5 Å resolution as defined by local resolution calculation in RELION 3.1. Masks were generated manually in Chimera[42] from RELION and CisTEM[43] maps. The use of SIDESPLITTER[44] extensions in RELION 3.1 were used in the reconstruction step in later rounds of refinement with a large mask to counter the effects of observed over-fitting to the detergent micelle and to ensure that all map density was included. Data processing details are shown in **Supplemental Figure 1**.

Model building was performed in RELION postprocessed maps and with blurred and sharpened maps from CCPEM[45] as needed. Model building was performed from a starting structure of TmrAB (PDBID: 6RAG[35]) in Coot[46] starting as a polyalanine model and real space refinement was performed using Phenix[47] against RELION postprocessed maps. Secondary structure and reference model restraints were used as was a high nonbonded energy term to ensure proper geometry. The ISOLDE[48] plug-in to ChimeraX[49] was used for difficult regions and to ensure correctly orientation of H-bonds. Placement of the Hoechst molecules was performed manually in Coot and then further refined with MD simulations (below) and Phenix. All figures were made using PyMol[50].

MD simulations

All simulations were carried out with NAMD 2.12[51] using the CHARMM36 force field[52,53] periodic boundary conditions, constant temperature (298 K) and semi-isotropic pressure (1 atm), and an integration time step of 2 fs. Force-field parameters for Hoechst-33342 were those developed in a previous study[30]. Long-range electrostatic interactions were calculated using PME, with a real-space cut-off of 12 Å; van der Waals interactions were computed with a Lennard-Jones potential cut-off at 12 Å with a smooth switching function taking effect at 10 Å. For computational efficiency, the considered in the simulations comprises only the transmembrane domain, i.e. extracellular (BmrD, residue 50-114) and intracellular domains (BmrC, residue 317-574; BmrD, residue 411-665) were truncated. Two molecules of the ligand Hoechst-33342 were included; the initial binding pose was produced by manual-fitting into the cryo-EM density map. The protein-ligand complex was embedded in a pre-equilibrated palmitoyl-oleoyl-phosphatidyl-choline bilayer, in a 100 mM NaCl buffer, using GRIFFIN[51]. Counterions were added to neutralize the net charge of the protein-ligand complex. The resulting system contain 206 POPC lipids and are ~90 x 90 x 126 Å in size, totaling ~106,000 atoms. The molecular system

was equilibrated following a staged protocol comprising a series of restrained simulations. The protocol consists of both positional and conformational restraints, gradually weakened over 100 ns, and individually applied to protein sidechains and backbone as well as the Hoechst molecules. Subsequently, two trajectories of 1 μs each were calculated, with no restraints.

Spin-labeling of BmrCD

For EPR spectroscopy, double-Cysteine mutants generated on the C-less background of BmrCD were eluted following Ni-NTA purification and labeled with 20-fold molar excess of 1-oxyl-2,2,5,5-tetramethylpyrroline-3-methyl methanethiosulfonate (Enzo Life Sciences) at room temperature in the dark over a 4 h period, after which protein samples were placed at 4 °C overnight (~15 h). The labeled protein samples in ß-DDM and LMNG were then separated from free label by size-exclusion chromatography on a Superdex 200 Increase column (Cytiva) in buffer containing 50 mM Tris-HCl, 150 mM NaCl, 10% (v/v) glycerol, pH 7.4 containing 0.05% β-DDM (ß-DDM samples) or 0.01% LMNG (digitonin samples). The samples in 0.01% LMNG containing buffer were then exchanged into digitonin buffer (50 mM Tris-HCl, 200 mM NaCl, 0.06% w/v digitonin, pH 7.4). The collected fractions of spin-labeled BmrCD mutants were concentrated using an Amicon Ultra-100 kDa centrifugal filters (Millipore), and the final concentration determined by absorbance at 280 nm (Mean extinction coefficient = 68077.5 M^{-1} cm^{-1}).

DEER sample preparation and DEER spectroscopy

Spin-labeled BmrCD mutants were concentrated to 70-100 μM using Amicon Ultra-100 kDa centrifugal filters (Millipore) and incubated with nucleotides or Hoechst-33342. The final concentrations of ATP, AMP-PNP, vanadate, $MgCl^{2+}$, and digitonin were 10 mM, 10 mM, 5 mM, 10 mM, and 0.25% respectively. Samples for DEER analysis were cryoprotected with 24% (v/v) glycerol. Post-hydrolysis (ADP-Vi) and turnover (H-ATP-$MgCl^{2}$) samples prepared in digitonin buffer were incubated at 37°C for 15 min and 1 min, respectively. β-DDM-solubilized protein samples were trapped in the post-hydrolysis state and with AMP-PNP by incubating at 30°C for 30 min. Turnover samples in β-DDM buffer conditions were incubated at 30 °C for 5min. Post-hydrolysis (ADP-Vi), turnover (H-ATP-$MgCl^{2+}$) and AMP-PNP reactions were stopped by flash freezing in a liquid nitrogen bath.

DEER spectroscopy was performed on an Elexsys E580 EPR spectrometer operating at Q-band frequency (33.9 GHz) equipped with a 40W Amp-Q amplifier (Bruker) with the dead-time free four-pulse sequence at 83 K[54,55]. The pulse lengths were 10 ns (p/2) and 20 ns (p) for the probe pulses and 40 ns for the pump pulse. The frequency separation was 73 MHz. Raw DEER decays were analyzed as described previously[14]. Briefly, primary DEER decays were analyzed using home-written software operating in the Matlab environment. The software carries out global analysis of the DEER decays obtained under different conditions for the same spin-labeled position. The distance distribution is assumed to consist of a sum of Gaussians, the number and population of which are determined based on a statistical criterion. Distance distributions on the BmrCD-QQ cryo-EM structure were predicted *in silico* using 1 ns molecular-dynamics simulations with dummy spin labels with default parameters using the DEER Spin-Pair

569 Distributor at the CHARMM-GUI website[56,57]. Experimental Data related to **Figures 1E**,
570 **2D**, and **3D** are reported in **Supplemental Figure 7**.

571

572 **ATPase assays**

573 The specific ATPase activities for wild-type (WT) and mutants of C-less BmrCD
574 were determined by an inorganic phosphate assay as previously described[14] with slight
575 modification. Briefly, BmrCD (20 µg) samples were incubated with increasing
576 concentrations of ATP at 30°C for 30 min under basal conditions (no Hoechst) or
577 presence of different concentrations of Hoechst. The reaction was stopped by adding 1%
578 SDS and the color was developed using a 1:1 solution of ammonium molybdate (2% in
579 1M HCl) and ascorbic acid (12% in 1M HCl). The absorbance of samples was measured
580 at a wavelength of 850 nm on a BioTek Synergy H4 microplate reader. The amount of
581 phosphate released was determined by comparison to a standard curve generated from
582 inorganic phosphate. The *V*max of WT and mutant C-less BmrCD was derived using the
583 Levenberg-Marquart nonlinear least squares fitting approach in Origin (OriginLab, Inc).

584

585 **ACKNOWLEDGEMENTS**

586 We thank Theo Humphries and other support staff at the Pacific Northwest Center
587 for Cryo-EM (PNCC) for assistance with cryo-EM data collection. We thank members of
588 the Tomasiak lab and Derek Claxton from the Mchaourab lab for critical reading of this
589 manuscript. This research was funded by the Division of Intramural Research of the
590 National Heart, Lung and Blood Institute (WZ and JDFG), National Institutes of Health
591 (NIH), USA and grants from the National Institute of General Medicine Sciences to T.M.
592 Tomasiak (R00 GM114245) and H.S. Mchaourab (GM 128087). Computational
593 resources were in part provided by the NIH HPC facility Biowulf.

REFERENCES AND NOTES

1. Holland, I. B. Rise and rise of the ABC transporter families. *Res. Microbiol.* **170**, 304–320 (2019).
2. Hofmann, S. *et al.* Conformation space of a heterodimeric ABC exporter under turnover conditions. *Nature* **571**, 580–583 (2019).
3. Kim, Y. & Chen, J. Molecular structure of human P-glycoprotein in the ATP-bound, outward-facing conformation. *Science (80-.).* **359**, 915–919 (2018).
4. Johnson, Z. L. & Chen, J. ATP Binding Enables Substrate Release from Multidrug Resistance Protein 1. *Cell* **172**, 81-89.e10 (2018).
5. Johnson, Z. L. & Chen, J. Structural Basis of Substrate Recognition by the Multidrug Resistance Protein MRP1. *Cell* **168**, 1075-1085.e9 (2017).
6. Choudhury, H. G. *et al.* Structure of an antibacterial peptide ATP-binding cassette transporter in a novel outward occluded state. *Proc. Natl. Acad. Sci. U. S. A.* **111**, 9145–9150 (2014).
7. Ward, A., Reyes, C. L., Yu, J., Roth, C. B. & Chang, G. Flexibility in the ABC transporter MsbA: Alternating access with a twist. *Proc. Natl. Acad. Sci. U. S. A.* **104**, 19005–19010 (2007).
8. Dawson, R. J. P. & Locher, K. P. Structure of a bacterial multidrug ABC transporter. *Nature* **443**, 180–185 (2006).
9. Mishra, S. *et al.* Conformational dynamics of the nucleotide binding domains and the power stroke of a heterodimeric ABC transporter. *Elife* **3**, e02740 (2014).
10. Tamaki, A., Ierano, C., Szakacs, G., Robey, R. W. & Bates, S. E. The controversial role of ABC transporters in clinical oncology. *Essays Biochem.* **50**, 209–232 (2011).
11. Seelig, A. P-Glycoprotein: One Mechanism, Many Tasks and the Consequences for Pharmacotherapy of Cancers. *Frontiers in Oncology* **10**, (2020).
12. Alam, A., Kowal, J., Broude, E., Roninson, I. & Locher, K. P. Structural insight into substrate and inhibitor discrimination by human P-glycoprotein. *Science (80-.).* **363**, 753–756 (2019).
13. Nosol, K. *et al.* Cryo-EM structures reveal distinct mechanisms of inhibition of the human multidrug transporter ABCB1. *Proc. Natl. Acad. Sci. U. S. A.* **117**, 26245–26253 (2020).
14. Mishra, S. *et al.* Conformational dynamics of the nucleotide binding domains and the power stroke of a heterodimeric ABC transporter. *Elife* **2014**, (2014).
15. Collauto, A., Mishra, S., Litvinov, A., Mchaourab, H. S. & Goldfarb, D. Direct Spectroscopic Detection of ATP Turnover Reveals Mechanistic Divergence of ABC Exporters Article Direct Spectroscopic Detection of ATP Turnover Reveals Mechanistic Divergence of ABC Exporters. *Structure* **25**, (2017).
16. Torres, C., Galián, C., Freiberg, C., Fantino, J.-R. & Jault, J.-M. The YheI/YheH heterodimer from Bacillus subtilis is a multidrug ABC transporter. *Biochim. Biophys. Acta - Biomembr.* **1788**, 615–622 (2009).
17. Zutz, A. *et al.* Asymmetric ATP Hydrolysis Cycle of the Heterodimeric Multidrug ABC Transport Complex TmrAB from *Thermus thermophilus*. *J. Biol. Chem.* **286**, 7104–7115 (2011).
18. Nöll, A. *et al.* Crystal structure and mechanistic basis of a functional homolog of the antigen transporter TAP. *Proc. Natl. Acad. Sci. U. S. A.* **114**, E438–E447

640 (2017).
641 19. Mi, W. *et al.* Structural basis of MsbA-mediated lipopolysaccharide transport.
642 *Nature* **549**, 233–237 (2017).
643 20. Ho, H. *et al.* Structural basis for dual-mode inhibition of the ABC transporter
644 MsbA. *Nature* **557**, 196–201 (2018).
645 21. Angiulli, G. *et al.* New approach for membrane protein reconstitution into
646 peptidiscs and basis for their adaptability to different proteins. *Elife* **9**, (2020).
647 22. Hohl, M. *et al.* Structural basis for allosteric cross-talk between the asymmetric
648 nucleotide binding sites of a heterodimeric ABC exporter. *Proc. Natl. Acad. Sci. U.*
649 *S. A.* **111**, 11025–11030 (2014).
650 23. Ward, A., Reyes, C. L., Yu, J., Roth, C. B. & Chang, G. Flexibility in the ABC
651 transporter MsbA: Alternating access with a twist. *Proc. Natl. Acad. Sci. U. S. A.*
652 **104**, 19005–19010 (2007).
653 24. Dawson, R. J. P. & Locher, K. P. Structure of a bacterial multidrug ABC
654 transporter. *Nature* **443**, 180–185 (2006).
655 25. Esser, L. *et al.* Structures of the Multidrug Transporter P-glycoprotein Reveal
656 Asymmetric ATP Binding and the Mechanism of Polyspecificity. *J. Biol. Chem.*
657 **292**, 446–461 (2017).
658 26. Hohl, M. *et al.* Structural basis for allosteric cross-talk between the asymmetric
659 nucleotide binding sites of a heterodimeric ABC exporter. *Proc. Natl. Acad. Sci. U.*
660 *S. A.* **111**, 11025–11030 (2014).
661 27. Timachi, M. H. *et al.* Exploring conformational equilibria of a heterodimeric ABC
662 transporter. *Elife* **6**, (2017).
663 28. Nosol, K. *et al.* Cryo-EM structures reveal distinct mechanisms of inhibition of the
664 human multidrug transporter ABCB1. *Proc. Natl. Acad. Sci. U. S. A.* **117**, 26245–
665 26253 (2020).
666 29. Alam, A., Kowal, J., Broude, E., Roninson, I. & Locher, K. P. Structural insight into
667 substrate and inhibitor discrimination by human P-glycoprotein. *Science (80-.).*
668 **363**, 753–756 (2019).
669 30. Debruycker, V. *et al.* An embedded lipid in the multidrug transporter LmrP
670 suggests a mechanism for polyspecificity. *Nat. Struct. Mol. Biol.* (2020).
671 doi:10.1038/s41594-020-0464-y
672 31. Madoori, P. K., Agustiandari, H., Driessen, A. J. M. & Thunnissen, A. M. W. H.
673 Structure of the transcriptional regulator LmrR and its mechanism of multidrug
674 recognition. *EMBO J.* **28**, 156–166 (2009).
675 32. Robinson, H. *et al.* 2'-Deoxyisoguanosine adopts more than one tautomer to form
676 base pairs with thymidine observed by high-resolution crystal structure analysis.
677 *Biochemistry* **37**, 10897–10905 (1998).
678 33. Verhalen, B. *et al.* Energy transduction and alternating access of the mammalian
679 ABC transporter P-glycoprotein. *Nature* **543**, 738–741 (2017).
680 34. Lusvarghi, S., Durell, S. R. & Ambudkar, S. V. Does the ATP-bound EQ mutant
681 reflect the pre- or post-ATP hydrolysis state in the catalytic cycle of human P-
682 glycoprotein (ABCB1)? *FEBS Lett.* (2021). doi:10.1002/1873-3468.14054
683 35. Hofmann, S. *et al.* Conformation space of a heterodimeric ABC exporter under
684 turnover conditions. *Nature* **571**, 580–583 (2019).
685 36. Jin, M. S., Oldham, M. L., Zhang, Q. & Chen, J. Crystal structure of the multidrug

686 transporter P-glycoprotein from Caenorhabditis elegans. *Nature* **490**, 566–569
687 (2012).
688 37. Dastvan, R., Mishra, S., Peskova, Y. B., Nakamoto, R. K. & Mchaourab, H. S.
689 Mechanism of allosteric modulation of P-glycoprotein by transport substrates and
690 inhibitors. *Science (80-.).* **364**, 689–692 (2019).
691 38. Siarheyeva, A., Liu, R. & Sharom, F. J. Characterization of an asymmetric
692 occluded state of P-glycoprotein with two bound nucleotides: Implications for
693 catalysis. *J. Biol. Chem.* **285**, 7575–7586 (2010).
694 39. Zivanov, J. *et al.* New tools for automated high-resolution cryo-EM structure
695 determination in RELION-3. *Elife* **7**, (2018).
696 40. Zivanov, J., Nakane, T. & Scheres, S. H. W. Estimation of high-order aberrations
697 and anisotropic magnification from cryo-EM data sets in RELION-3.1. *IUCrJ* **7**,
698 253–267 (2020).
699 41. Rohou, A. & Grigorieff, N. CTFFIND4: Fast and accurate defocus estimation from
700 electron micrographs. *J. Struct. Biol.* **192**, 216–221 (2015).
701 42. Pettersen, E. F. *et al.* UCSF Chimera - A visualization system for exploratory
702 research and analysis. *J. Comput. Chem.* **25**, 1605–1612 (2004).
703 43. Grant, T., Rohou, A. & Grigorieff, N. cisTEM, user-friendly software for single-
704 particle image processing. *Elife* **7**, (2018).
705 44. Ramlaul, K., Palmer, C. M., Nakane, T. & Aylett, C. H. S. Mitigating local over-
706 fitting during single particle reconstruction with SIDESPLITTER. *J. Struct. Biol.*
707 **211**, (2020).
708 45. Wood, C. *et al.* Collaborative computational project for electron cryo-microscopy.
709 *Acta Crystallogr. Sect. D Biol. Crystallogr.* **71**, 123–126 (2015).
710 46. Emsley, P., Lohkamp, B., Scott, W. G. & Cowtan, K. Features and development of
711 Coot. *Acta Crystallogr. Sect. D Biol. Crystallogr.* **66**, 486–501 (2010).
712 47. Liebschner, D. *et al.* Macromolecular structure determination using X-rays,
713 neutrons and electrons: Recent developments in Phenix. *Acta Crystallogr. Sect. D*
714 *Struct. Biol.* **75**, 861–877 (2019).
715 48. Croll, T. I. ISOLDE: A physically realistic environment for model building into low-
716 resolution electron-density maps. *Acta Crystallogr. Sect. D Struct. Biol.* **74**, 519–
717 530 (2018).
718 49. Pettersen, E. F. *et al.* UCSF ChimeraX: Structure visualization for researchers,
719 educators, and developers. *Protein Sci.* **30**, 70–82 (2021).
720 50. The PyMOL Molecular Graphics System, Version 2.0 Schrödinger, LLC.
721 51. Staritzbichler, R., Anselmi, C., Forrest, L. R. & Faraldo-Gómez, J. D. GRIFFIN: A
722 versatile methodology for optimization of protein-lipid interfaces for membrane
723 protein simulations. *J. Chem. Theory Comput.* **7**, 1167–1176 (2011).
724 52. Best, R. B. *et al.* Optimization of the additive CHARMM all-atom protein force field
725 targeting improved sampling of the backbone φ, ψ and side-chain χ1 and χ2
726 Dihedral Angles. *J. Chem. Theory Comput.* **8**, 3257–3273 (2012).
727 53. Klauda, J. B. *et al.* Update of the CHARMM All-Atom Additive Force Field for
728 Lipids: Validation on Six Lipid Types. *J. Phys. Chem. B* **114**, 7830–7843 (2010).
729 54. Jeschke, G. DEER Distance Measurements on Proteins. *Annu. Rev. Phys. Chem.*
730 **63**, 419–446 (2012).
731 55. Jeschke, G. & Polyhach, Y. Distance measurements on spin-labelled

biomacromolecules by pulsed electron paramagnetic resonance. *Phys. Chem. Chem. Phys.* **9**, 1895–1910 (2007).

56. Jo, S., Kim, T., Iyer, V. G. & Im, W. CHARMM-GUI: A web-based graphical user interface for CHARMM. *J. Comput. Chem.* **29**, 1859–1865 (2008).

57. Qi, Y. *et al.* CHARMM-GUI DEER facilitator for spin-pair distance distribution calculations and preparation of restrained-ensemble molecular dynamics simulations. *J. Comput. Chem.* **41**, 415–420 (2020).

TABLES

Table 1. Data collection and refinement statistics

Refinement		
Lengths (Å)	101.66, 151.44, 97.43	
Atoms	19813 (Hydrogens: 9926)	
Residues	Protein: 1236	
Water	0	
Resolution (Å)	3.5	
Resolution Estimates (Å)	Masked	Unmasked
d FSC model (0/0.143/0.5) (Å)	2.8/3.1/6.1	3.0/3.1/6.4
B-factors ($Å^2$)		
Iso/Aniso (#)	9887/0	
Protein (min/max/mean)	12.04/113.39/61.00	
Bonds (RMSD)		
Length (Å) (# > 4σ)	0.007	
Angles (°) (# > 4σ)	1.199	
Validation		
MolProbity score	1.46	
Clash score	0.86	
Ramachandran plot (%)		
Outliers	0	
Allowed	9.0	
Favored	90.02	
Rotamer outliers (%)	1.54	
Model vs. Data		
CC (mask)	0.69	
CC (box)	0.61	
CC (peaks)	0.51	
CC (volume)	0.65	

FIGURES

Figure 1

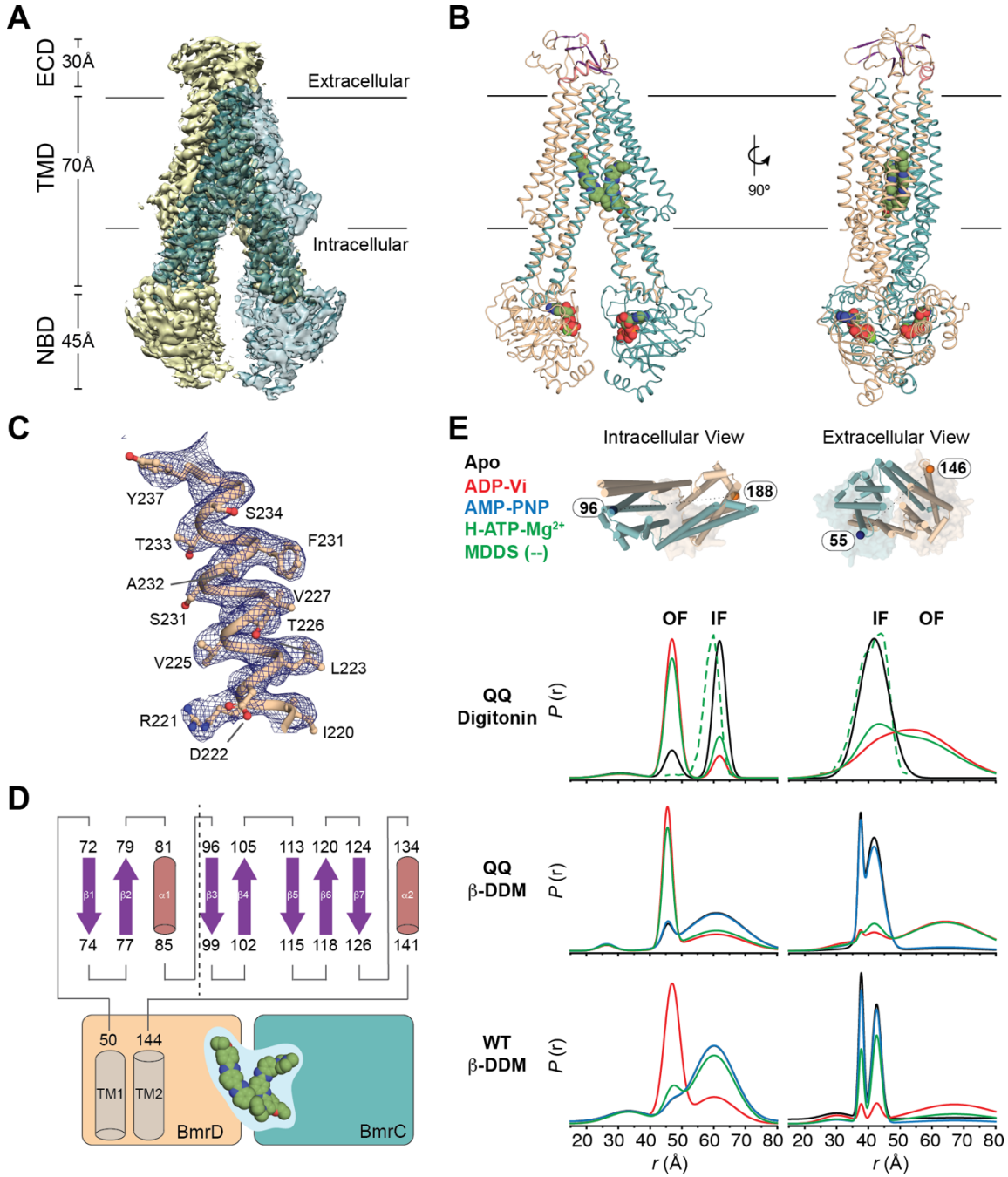

Figure 1. Structure of BmrCD$^{D500Q/E592Q}$ in complex Hoecsht-33342 and ATP. A) Cryo-EM map and **B)** model of BmrCD$^{D500Q/E592Q}$ (BmrCD-QQ) bound to ATP and Hoecsht-33342 (BmrCD-QQ$^{H/ATP}$) highlighting the geometry and arrangement of the transmembrane domains (TMDs) and nucleotide binding domains (NBDs) relative to the extracellular domain insertion (ECD) and the membrane. **C)** Representative density of the

754 3.5Å resolution structure show in (***A***) and model corresponding to transmembrane helix
755 3 from BmrD ($TM3^{D}$). **D)** Topology of the ECD observed in BmrCD-$QQ^{H/ATP}$ relative to the
756 TMD. **E)** DEER distance measurements for spin label pairs on the intracellular and
757 extracellular regions of the TMD in the Cysteine-free background (WT*) or the QQ mutant
758 of BmrCD and in the presence of different substrates. The MDDS-derived distance
759 distributions calculated for the cryo-EM model in (***B***) is overlaid with the DEER derived
760 distance distributions.

Figure 2

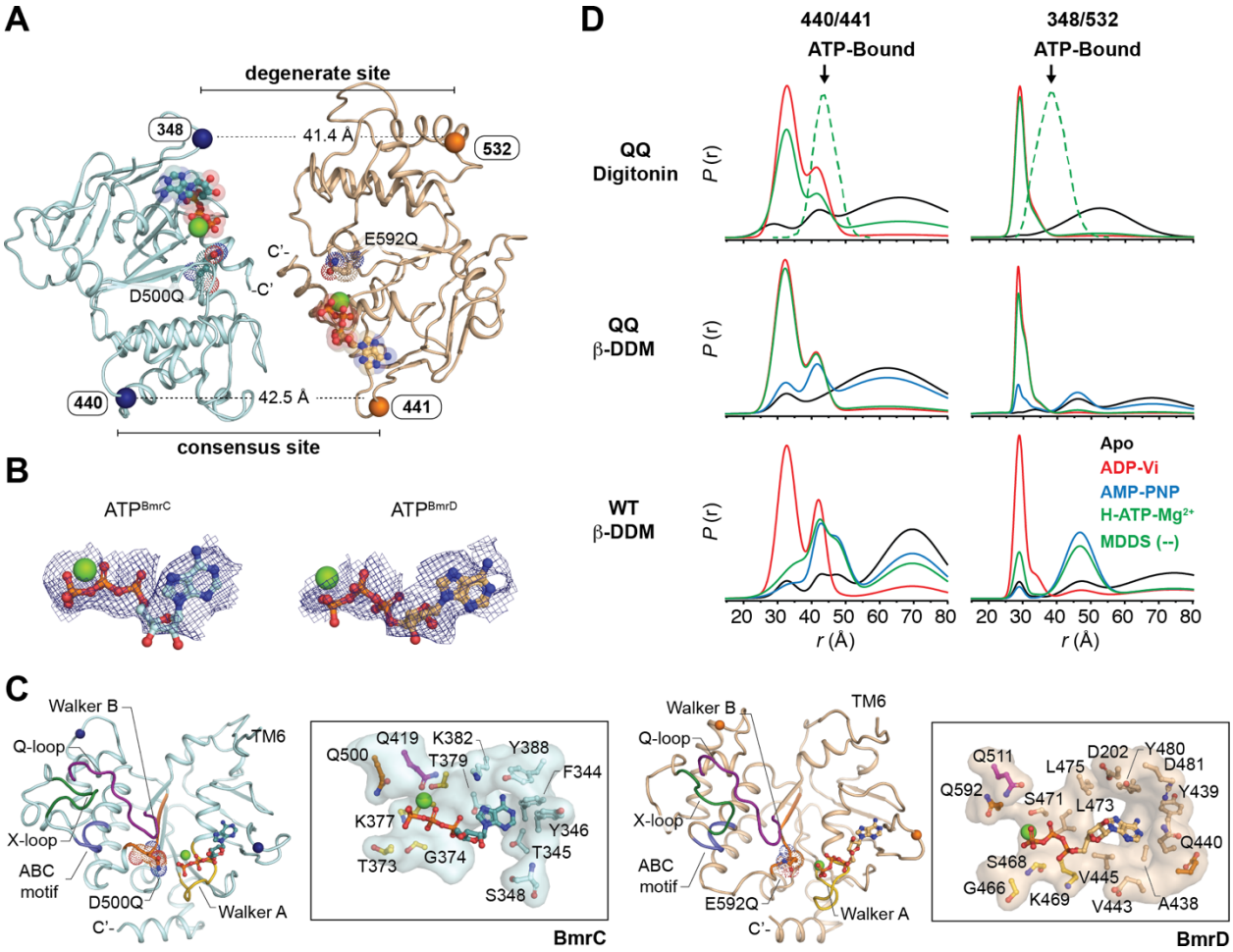

Figure 2. Symmetric geometry of ATP-bound NBSs in BmrCD-QQ$^{H/ATP}$. A) Overview of the nucleotide binding domains in the cryo-EM structure of BmrCD-QQ$^{H/ATP}$. **B)** Electron Potenial Density corresponding to ATP bound in the BmrC (left) and BmrD (right) chains with symmetric geometries. **C)** Comparison of NBD secondary structure in BmrC (left) and BmrD (right) highlighting the architecture of conserved motifs and the orientations of ATP molecules relative to the position of the catalytic base (D500Q in BmrC; E592Q in BmrD)**.** In the inset, an overview of the atomic features of the ATP binding pockets of each are shown with residues from conserved motifs colored the same. The orientations shown are of the same view in which BmrD was superimposed onto BmrC to highlight the symmetry of the ATP conformation in each. **D)** DEER distance distributions for spin labeled pairs in the BmrCD consensus (440/441) and degenerate (348/532) nucleotide binding sites under varying conditions. Superimposed in dashed green lines (MDDS) are the distance distributions predicted by the structure.

Figure 3

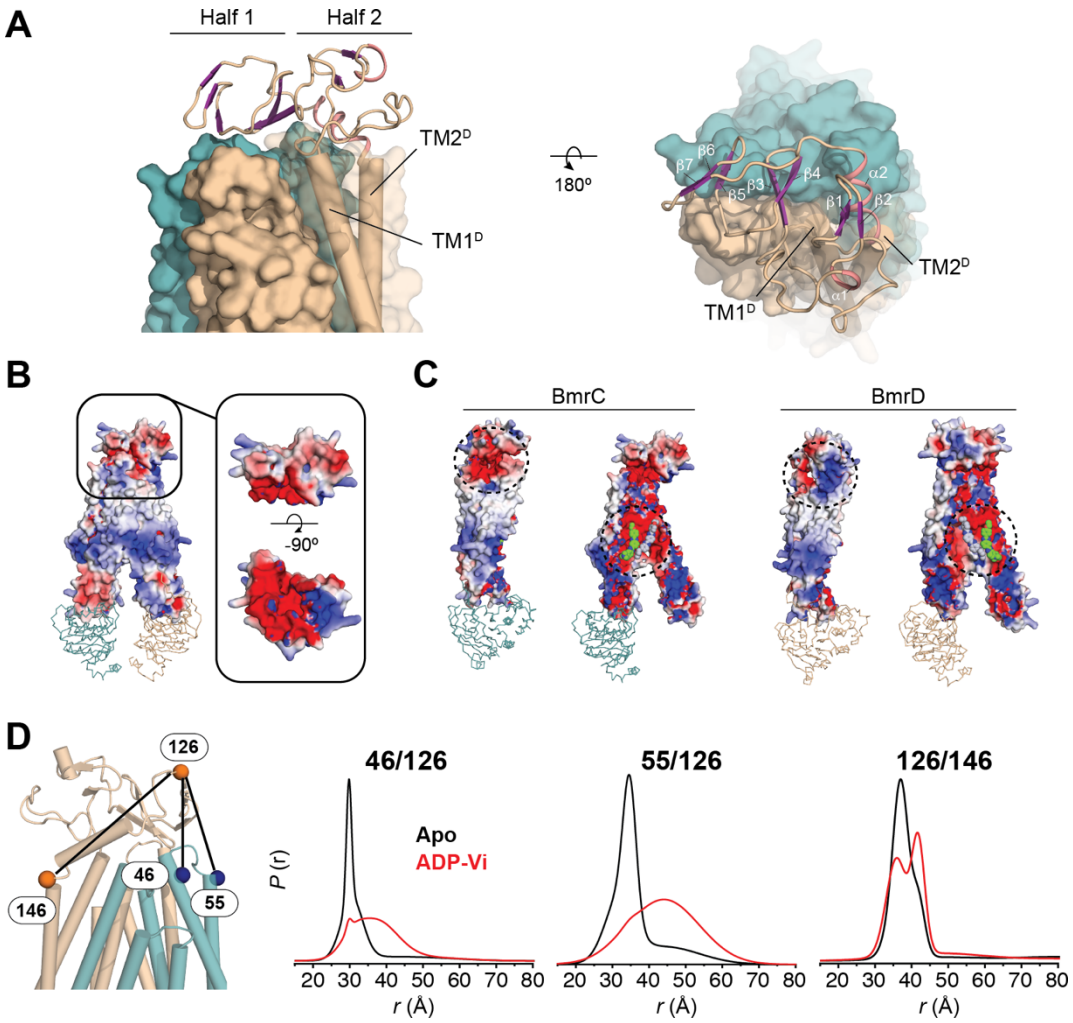

Figure 3. A dynamic role of the ECD in BmrCD-QQ$^{H/ATP}$ catalysis. A) Orientation of the ECD in BmrCD-QQ$^{H/ATP}$ relative to its TMD. **B)** Electrostatic distribution over the surface of the BmrCD-QQ$^{H/ATP}$. **C)** ECD and its interactions with BmrC (left) and BmrD (right). **D)** ECD/TMD spin labeled pairs generated in the BmrCD WT* to monitor the ATP-dependent dynamics of the ECD.

786 **Figure 4**

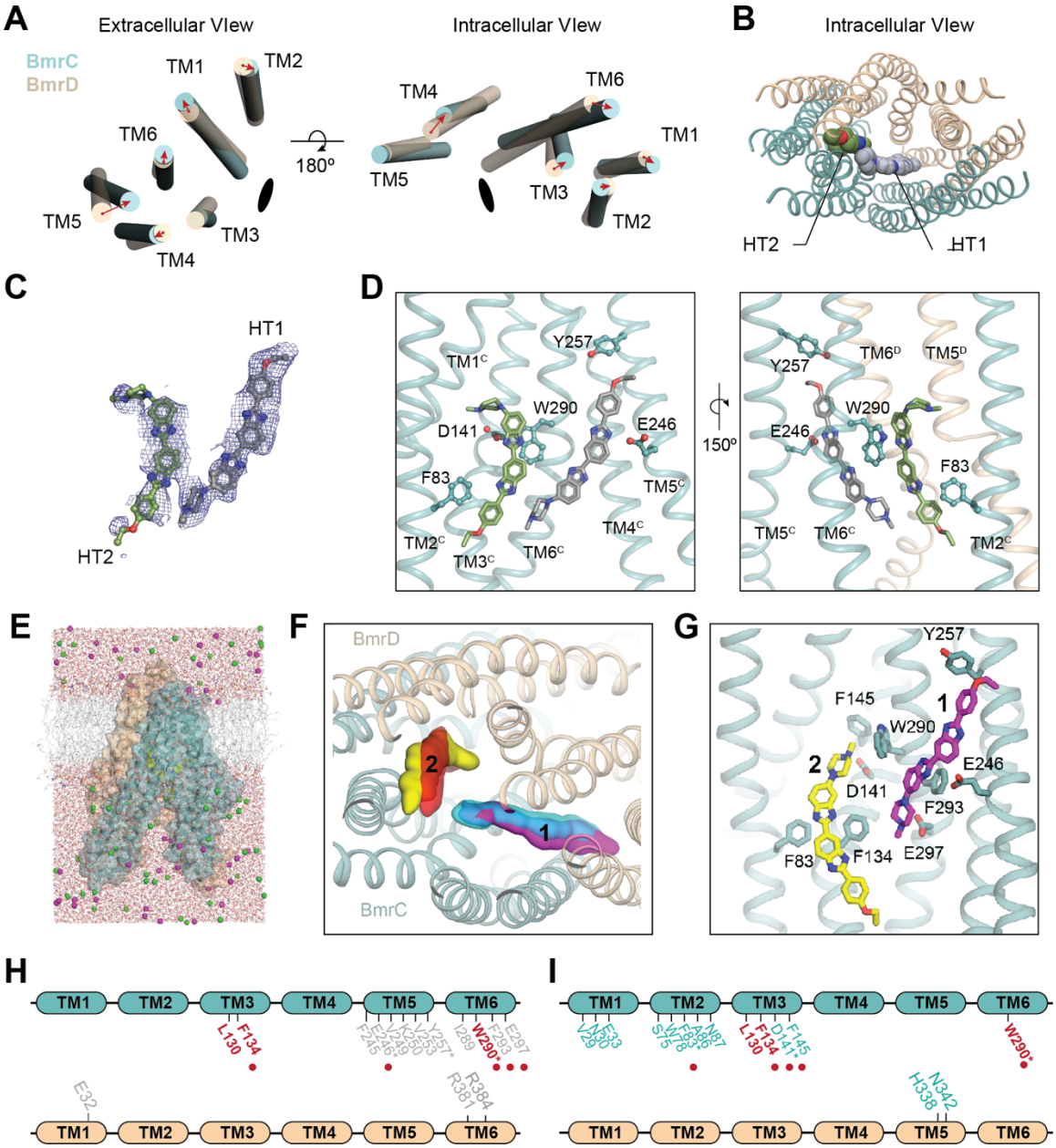

787

788 **Figure 4. Asymmetric binding of Hoecsht-33342 in BmrCD-QQ$^{H/ATP}$. A)** Superposition
789 of BmrD transmembrane helices (TM1-6) onto BmrC shown from the extracellular (left)
790 and intracellular (right) gates to highlight asymmetry in the TM arrangement observed in
791 the structure of BmrCD. Red arrows correspond to the movement of each TM in BmrC
792 relative to its position in BmrD. Black ellipse corresponds to the symmetry axis around
793 which BmrD was rotated during superposition. **B**) Intracellular view of the arrangement of
794 two molecules of Hoecsht-33342 (HT1 and HT2) modelled in the TMD of BmrCD. **C)**
795 Electron potential density observed corresponding to HT1 and HT2 and the **D)** their
796 positioning inside of the binding pocket. **E)** All-atom simulation system, comprising the
797 transmembrane domain of an apo model of BmrCD with two Hoechst molecules placed

into the proposed binding site, in a POPC lipid bilayer and 100 mM NaCl (BmrC, blue surface/cartoons; BrmD, orange surface/cartoons; Hoechst, yellow spheres; lipid, gray lines; water, red lines; sodium, magenta spheres; chloride, green spheres). **F)** Density maps calculated from the MD trajectories for each Hoechst molecule are overlaid onto the starting cryo-EM structure (magenta/red surfaces derive from one trajectory and cyan/yellow from the other). **G)** Snapshot representative of the calculated density maps, highlighting the configuration of the two Hoechst molecules and their seemingly most significant sidechain contacts with BmrC. Hydrogen atoms are omitted for clarity. Probability distributions for each of these interaction distances are shown in Supp. Fig. 6. The HT1 and HT2 specific interactions are summarized in **H)** and **I)**, respectively and mapped onto the respective chains colored the same as in (**A**) and (**B**). Residues colored in red are observed for both molecules. Residues with an asterisk were mutated in the study here. Equivalent residues in BmrC and BmrD are underlined.

Figure 5

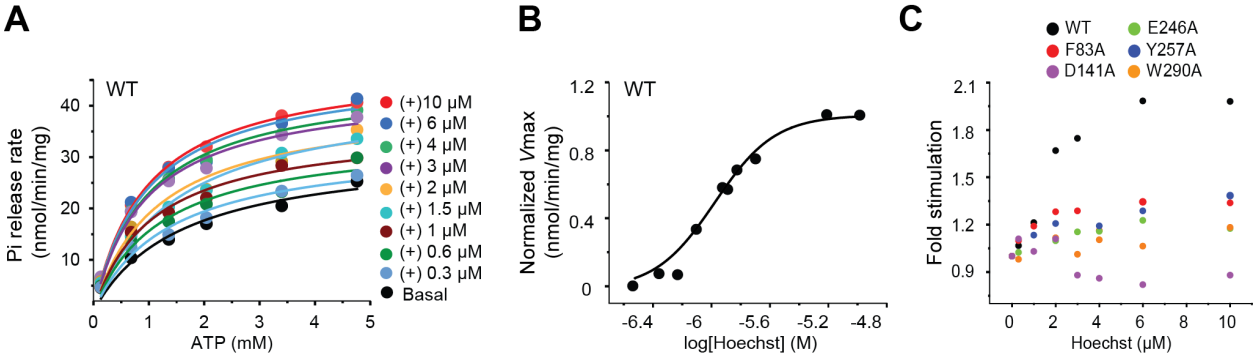

Figure 5. Cooperative stimulation of ATP turnover by Hoechst-33342. A) Hoechst-33342 concentration dependent stimulation of ATPase activity in wild-type (WT) C-less BmrCD. **B)** Dose-response curve for Hoechst-mediated stimulation of ATpase activity highlighting cooperativity in WT C-less BmrCD. The data is the average of two biological repeats and six technical repeats. **C)** Comparison of Hoechst-stimulated ATPase activity relative to basal activity (fold stimulation) in WT* and alanine mutants of BmrCD. Mutants selected are of a subset of residues observed interacting with Hoechst-33342 in the BmrCD-QQ$^{H/ATP}$ cryo-EM structure.

824 **Supplementary Materials**

825 **Supplemental Tables**

826

827 **Supplemental Table 1. RMSD analysis of domain architecture in BmrCD**

	RMSD (Å)
TMD	3.07
TM1	2.2
TM2	1.41
TM3	8.58
TM4	4.99
TM5	2.07
TM6	1.86
ICLs	2.36
ICL1	1.32
ICL2	1.19
NBD	2.85

828 TMD: transmembrane domain; ICLs: intracellular loops; NBD: nucleotide-binding domain

829

830 **Supplemental Table 2. BmrCD vs. TmrAB RMSD Analysis**

			TMD RMSD (Å)				NBD RMSD (Å)	
		overall	A vs. D	B vs. D	A vs. C	B vs. C	A vs. D	B vs. C
IO	*5mkk*	*5.025*	2.639	3.513	3.776	2.775	2.099	1.232
	6raf	5.424	2.285	3.612	4.247	3.813	2.232	1.394
	6rag	3.624	2.253	2.442	3.133	2.002	1.851	1.55
	6ran	3.404	2.159	2.293	2.927	1.882	2.316	1.467
OO	*6rah*	7.589	5.976	6.563	6.948	6.268	2.765	1.434
	6rai	6.731	4.731	5.297	5.557	3.097	2.683	1.592
	6raj	7.607	5.937	6.499	6.943	6.407	2.773	1.648
	6rak	6.757	4.799	5.371	5.696	3.291	2.687	1.627
	6ral	6.399	4.381	4.899	5.225	3.011	2.824	1.593
	6ram	6.059	4.029	4.271	4.822	2.887	2.712	1.373

831 IO: inward-facing open; OO: outward-facing open or occluded

832

833

834 **Supplemental Figures**

835 **Supplementary Figure 1**

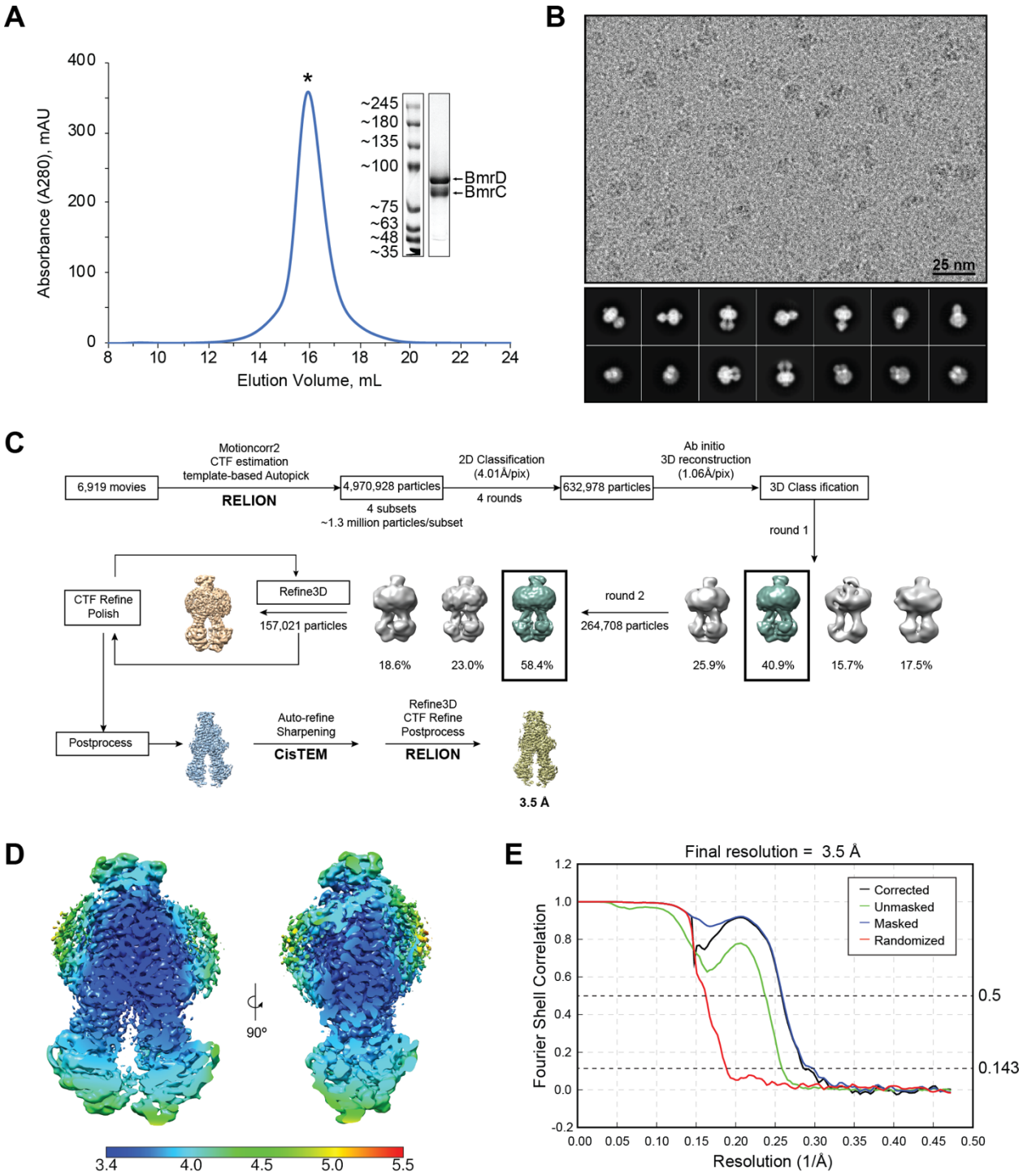

836

837 **Supplementary Figure 1. Cryo-EM data processing of BmrCD-QQ in the Hoechst-**
838 **33342 and ATP/Mg bound state. A)** Chromatogram and SDS-PAGE analysis of the
839 peak composition for BmrCD-QQ purified by size exclusion chromatography over a

840 Superose 6 column equilibrated in 0.02% digitonin containing buffer prior to sample
841 preparation for cryo-EM data collection. **B)** Representative micrograph and 2D
842 classification rsults from cryo-EM data collected for BmrCD-QQ in the presence of
843 equimolar ATP/$MgCl_2$ and excess Hoechst-33342. **C)** Flowchart of data processing in
844 RELION 3.1[40] and CisTEM[43]. **D)** A slice through the EM volume colored according to local
845 resolution. **E)** FSC curves calculated by RELION 3.1.
846

847 **Supplementary Figure 2**

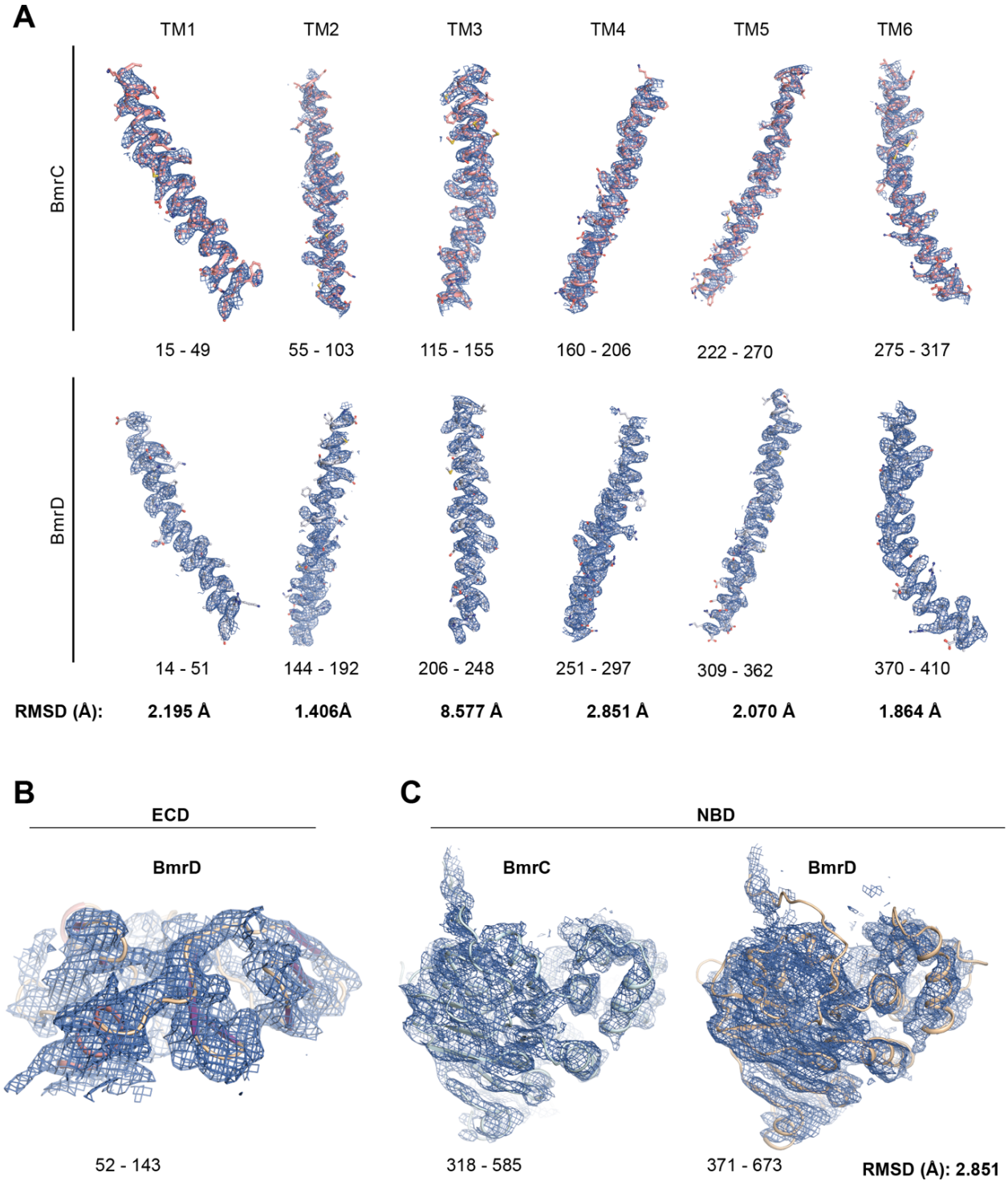

848

849 **Supplementary Figure 2. Cryo-EM map data quality.** Model and corresponding density
850 of BmrCD-QQ **A)** transmembrane helices (TM1-6), **B)** extracellular domain (ECD), and

851 **C)** nucleotide binding domains (NBD). Root mean square deviations (RMSD) are reported
852 for Cα alignment of the corresponding regions.
853

854 **Supplementary Figure 3**

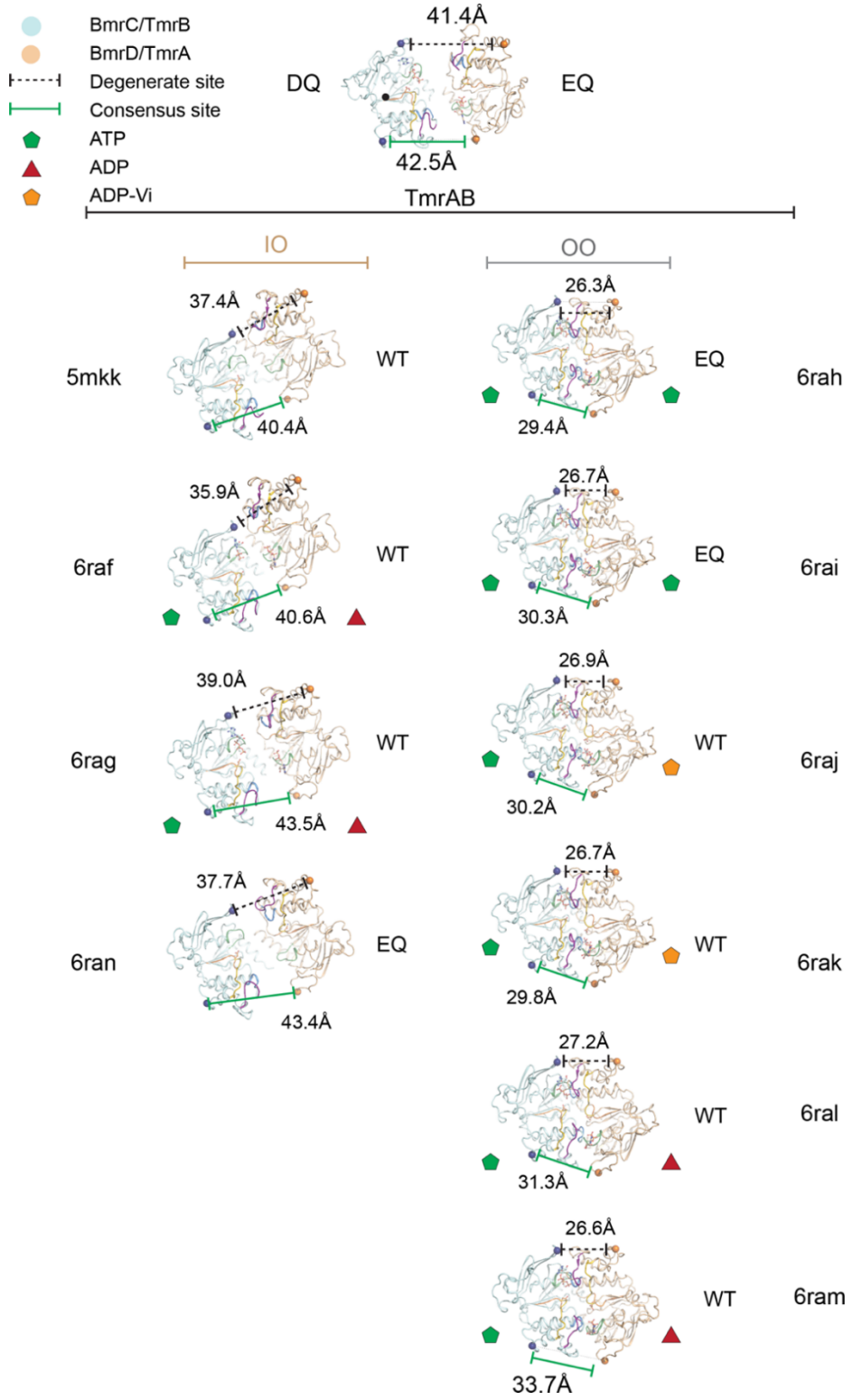

855

856

857 **Supplementary Figure 3. Analysis of NBD symmetry in BmrCD compared to**
858 **TmrAB.** Comparison of NBD geometry between BmrCD and different states of TmrAB
859 determined by x-ray crystallography (PDB ID: 5mkk[18]) and cryo-EM[2]. The noncanonical
860 NBD in BmrC and TmrB are colored the same (*cyan*), whereas the consensus NBDs of
861 BmrD and TmrA are colored the same (*orange*). The orientations shown are relative to
862 the BmrCD in which TmrB was aligned to BmrC (marked with a black dot in the center to
863 denote the reference orientation). Structures of TmrAB are shown grouped by
864 architectures adopting inward-facing open states (IO) or outward-facing states (OO).

865 **Supplementary Figure 4**

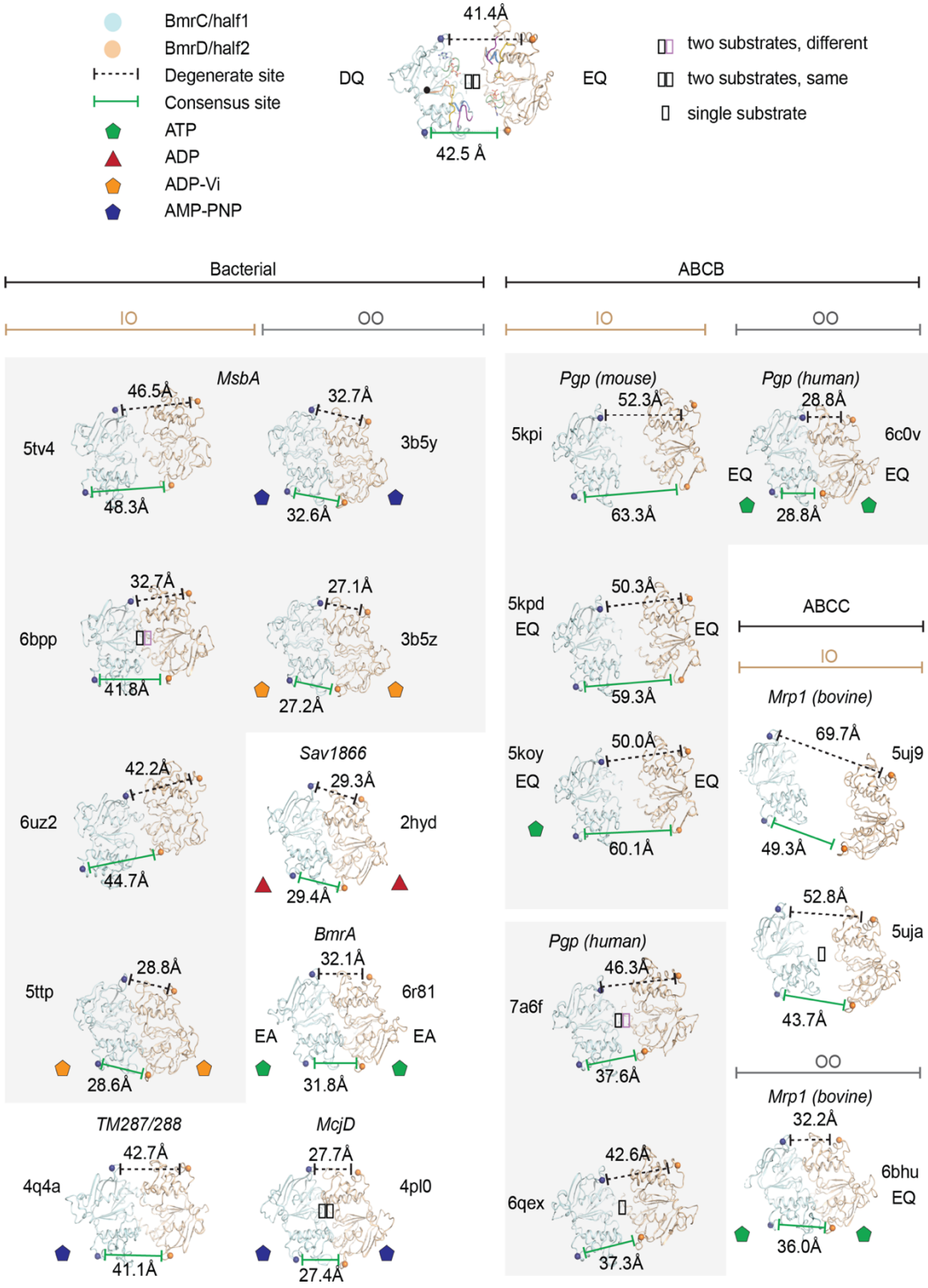

866

867 **Supplementary Figure 4. Analysis of NBD symmetry between BmrCD and other**
868 **representative ABC transporters.** Comparison of NBD geometry between BmrCD and
869 structures of related ABC transporters from bacteria (MsbA PDB IDs: 5TV4[19], 6BPP[20],
870 6UZ2[21], 3B5Y[23], and 3B5Z[23], TM2987/288 PDB ID: 2HYD[24], BmrA PDB ID: 6R81
871 (unpublished); McjD PDB ID: 4PL0[6]) as well as from the ABCB and ABCC families . The
872 noncanonical NBDs, or the first NBD in homomeric or single polypeptide transporters, are
873 colored the same (*cyan*), whereas the consensus NBDs, or the second NBD in
874 homomeric or single polypeptide transporter, are colored the same (*orange*). The
875 orientations shown are relative to the BmrCD in which TmrB was aligned to BmrC (marked
876 with a black dot in the center to denote the reference orientation). Structures of TmrAB
877 are shown grouped by architectures adopting inward-facing open states (IO) or outward-
878 facing states (OO).
879

880 **Supplemental Figure 5**

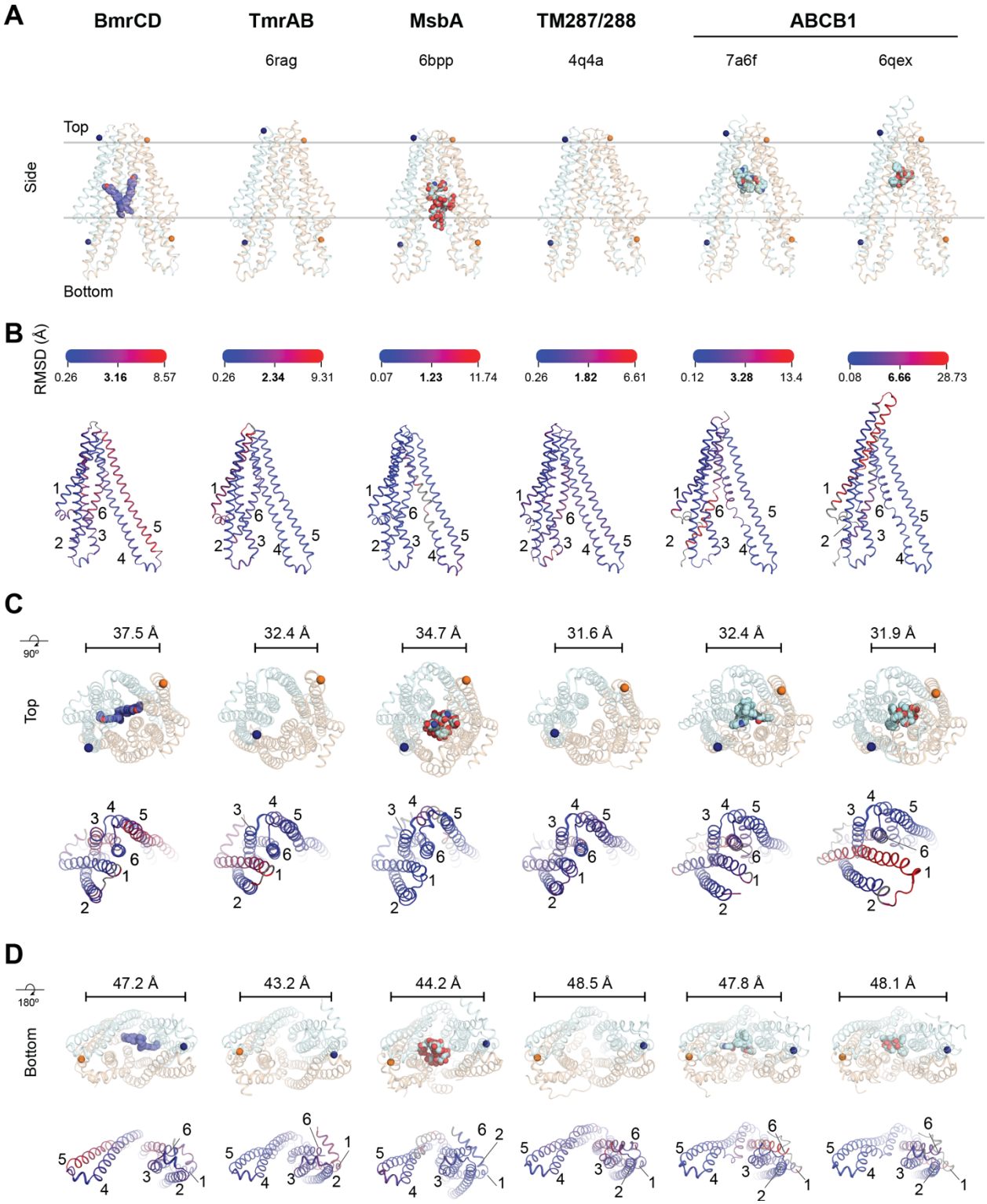

881

882 **Supplemental Figure 5. Analysis of BmrCD TMD in comparison to closely related**
883 **ABC exporters in the inward-facing architecture. A)** Overview of the transmembrane

884 domain (TMD) geometry in BmrCD and related inward-facing states of related prokaryotic
885 (PDB IDs: 6rag[2], 6bpp[20], and 4q4a[22]) and human ABC transporters bound with inhibitor
886 (PDB ID: 7a6f[13]) or substrate (PDB ID: 6qex[12]). The extracellular domain of BmrD and
887 both nucleotide binding domains have been omitted for clarity. Sites on the extracellular
888 and intracellular gates labeled for DEER experiments in BmrCD and the homologous
889 residues in the related exporters are shown as spheres and colored the same as Figures
890 1 of the main text, where the non-canonical nucleotide-binding site (NBS) containing half
891 are colored cyan (BmrC in BmrCD), and the canonical NBS containing half are colored
892 orange (BmrD in BmrCD). **B)** The Cα RMSD resulting from superposition of each halve
893 of the TMD region in each structure is mapped onto the structure of the non-canonical
894 half. The scale bar above represents the minimum, median, and maximum RMSD
895 calculated for each superposition. The geometry and RMSD distribution in each are
896 shown for the **C)** outside-facing (top) and **D)** inside-facing (bottom) regions of the TMDs
897 to highlight the variation in asymmetry in each structure. Numbers in the RMSD
898 representation correspond to the transmembrane helix number.
899

Supplemental Figure 6

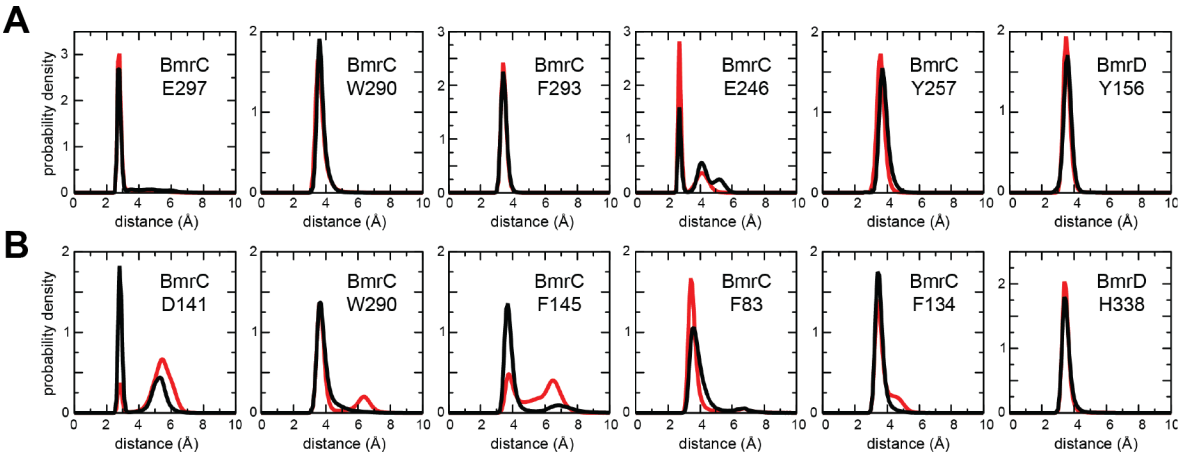

Supplemental Figure 6. Examination of the Hoechst binding pose with MD simulations. Data is shown for two independent MD trajectories (black, red) of the BmrCD construct shown in Fig. 4G, with two Hoechst molecules bound. **A)** Quantification of ionic and aromatic interactions between Hoechst molecule '1' and residues in BrmC, in terms of probability distributions of the minimum distance between the ligand and each sidechain (excluding hydrogens). The only significant contact of Hoechst molecule '1' with BrmD is also indicated. **B)** Same as **A)**, for molecule '2'.

Supplemental Figure 7

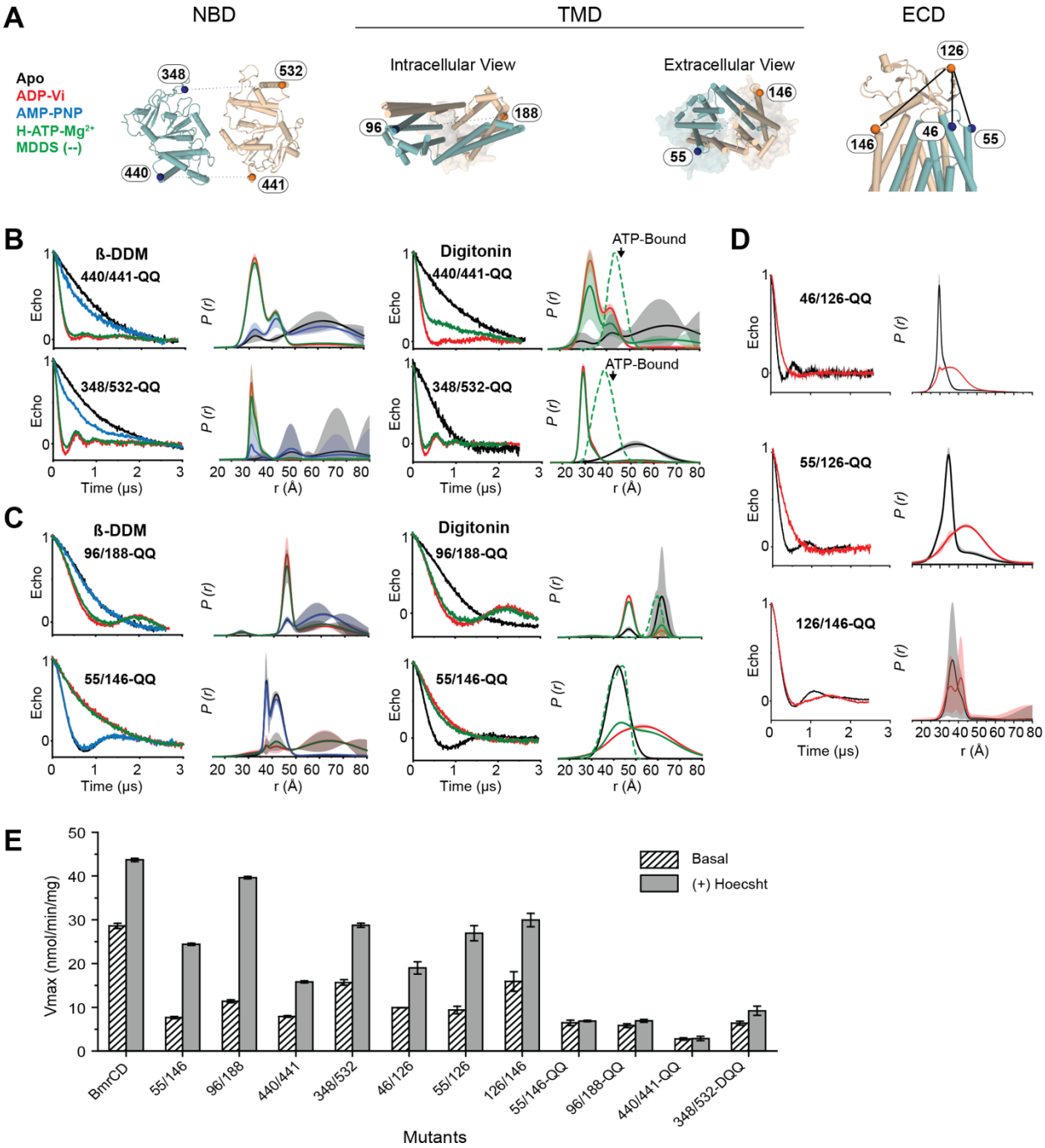

Supplemental Figure 7. A) Cartoon representation of BmrCD highlighting the position of spin-labeled cysteine pairs generated in the nucleotide binding domain (NBD), transmembrane domain (TMD), and the extracellular domain (ECD). DEER decay signals and distance distributions for spin-labeled Cysteine pairs generated in the **B)** NBD, **C)** TMD, and **D)** ECD for C-less BmrCD. The shaded regions represent confidence bands. **E)** Quantification of maximal ATPase rates (*V*max) in wild-type and C-less spin-label mutants of BmrCD.